Thermophysical properties of water using reactive force fields

Oliver R. Gittus[1] and Fernando Bresme[1, a)]

Department of Chemistry, Molecular Sciences Research Hub Imperial College, London W12 0BZ, United Kingdom.

The widescale importance and rich phenomenology of water continue to motivate the development of computational models. ReaxFF force fields incorporate many characteristics desirable for modelling aqueous systems: molecular flexibility, polarization and chemical reactivity (bond formation and breaking). However, their ability to model the general properties of water has not been evaluated in detail. We present comprehensive benchmarks of the thermophysical properties of water for two ReaxFF models, the water-2017 and CHON-2017_weak force fields. These include structural, electrostatic, vibrational, thermodynamic, coexistence, and transport properties at ambient conditions (300 K and 0.997 g cm^{-3}) and along the standard pressure (1 bar) isobar. Overall, CHON-2017_weak predicts more accurate thermophysical properties than the water-2017 force field. Based on our results we recommend potential avenues for improvement: the dipole moment to quadrupole moment ratio, the self-diffusion coefficient especially for water-2017, and the gas phase vibrational frequencies with the aim to improve the vibrational properties of liquid water.

I. INTRODUCTION

Water plays a central role in our lives: it is ubiquitous in nature and industry, and by definition hosts the entirety of aqueous chemistry. It is therefore unsurprising that an accurate description of water is a long-standing goal of computational chemistry and physics. To this end a vast number of water models have been developed, each with its own set of strengths, limitations and scope.

Despite their simplicity, empirical force fields have achieved great success in reproducing the structural, thermodynamic and transport properties of liquid water over a broad range of temperatures and pressures. Arguably the most successful general purpose water model for thermodynamic properties,[1] TIP4P/2005[2] reproduces the phase diagram and anomalous properties of water fairly accurately.[1] Another rigid force field, SPC/E[3] remains one of the most popular models for liquid water, and predicts a dielectric constant in better agreement with experiment. Flexible models such as TIP4P/2005f, SPCFw[4] and mSPCFw[5] incorporate intramolecular degrees of freedom through O-H bond and H-O-H angle potentials. Early central force models of water incorporated for the first time self-dissociation effects and flexibility in an empirical force field. These force fields predict thermophysical properties that are in general, in good agreement with experiments.[6,7] Explicitly including polarization in water simulations remains an open challenge, with classical approaches either modelling charge redistribution within each atom (e.g. induced dipole and Drude oscillator methods), or charge flow between atoms (e.g. fluctuating charge models).[8–11] A key motivation for incorporating polarization effects is the accurate description of water's dipole moment in both the vapour and liquid phases using a single force field. Many-body potentials go beyond the pairwise approximation, explicitly considering higher-order terms in the interaction energy.[12] The mW model is a widely used coarse grained model of water that explicitly incorporates three body terms[13]. The majority of the empirical water models developed to date, with the exception of central force models, are non-dissociative; they are unable to describe the formation and breaking of chemical bonds.

Ab initio methods are able to model bond dissociation, but remain prohibitively expensive for many applications. Even so, the accurate description of water by DFT is a work in progress, with the Jacob's ladder of approximations providing more accurate but costly descriptions at each progressive rung.[14] Many popular GGAs underestimate the bulk density of water,[14] and predict that the density of ice is higher than water (ice sinks in water).[14–16] When modelling water at the experimental density of 1 g cm^{-3}, GGA functionals typically predict an overstructured liquid with a low self-diffusion coefficient.[14] These problems persist even for hybrid functionals and when accounting for nuclear quantum effects (NQEs).[14,15,17] Dispersion corrections help ameliorate these deficiencies because semi-local functionals do not describe the long-range electron correlations that gives rise to the asymptotic r^{-6} decay in interaction energy.[14] meta-GGA functionals can offer an improved description of structure and dynamics,[16,18,19] and the SCAN functional notably predicts the correct order of water and ice densities.[16] A proportion of exact exchange (i.e. hybrid functionals) together with a well-chosen treatment of dispersion may provide an accurate description of liquid water at ambient conditions, but this level of theory is limited to simulations of around 100s of atoms for 10s of picoseconds, even with today's state-of-the-art supercomputers.

Semi-empirical methods (e.g. DFTB and MOPAC) and reactive force fields (RFFs) (also called dissociative force fields) offer more computationally feasible routes to modelling chemical reactivity. Of the latter, ReaxFF models can accommodate simulations of many (10s of) thousands of atoms on the nanosecond timescale using (state-of-the-art) high-performance computing facilities. The first-generation ReaxFF water force field was parameterized against DFT (X3LYP/6-311G**) data, primarily fitting to energetic benchmarks (such as dissociation curves, binding energies and reaction barriers) for single molecules, dimers, clusters and

---

a)Electronic mail: Author to whom correspondence should be addressed: f.bresme@imperial.ac.uk

ice, while also targetting properties of the bulk liquid when deciding on the final parameter set.[20] The first-generation ReaxFF force field describes water dissociation and the structural migration of solvated protons (the Grotthus mechanism), but underestimates the bulk density of liquid water by ∼8% at 298 K and ambient pressure,[21] and predicts the incorrect order of H_2O/H_3O^+/OH^- diffusion coefficients.[20] The second-generation ReaxFF force field (water-2017) remedied these deficiencies by including the experimental density and H_2O/H_3O^+/OH^- diffusion coefficients as training data in the reparameterization of the first-generation force field.[21] Additional DFT reference data was also included to improve the structure of the hydrated OH^- ion. Another ReaxFF force field designed to model water, CHON-2017_weak is a reparameterization of the protein-2013[22] RFF (and thus indirectly of the first-generation water RFF) that improves the description of weak interactions in condensed phase functionalized hydrocarbon/water systems.[23]

The water-2017 and CHON-2017_weak force fields have been used to model a wide range of phenomena in water and water-containing systems, for example: hydrogen bonding in supercritical water[24]; water isotope dynamics[25]; water-graphene/graphene oxide interfaces[26–29]; anion exchange membranes[30,31]; and polymer biodegradation[32]. Benchmarks of CHON-2017_weak water at higher than ambient temperatures and pressures (sub- and supercritical) have already been performed.[33] However, many important thermodynamic and transport properties have not been calculated at "ambient" (300 K) conditions, or along the standard pressure 1 bar isobar. Additionally, there have been recent efforts to refine the predicted thermodynamic properties of ReaxFF water through the improved description of electrostatics and long-range dispersion interactions.[34,35] More comprehensive benchmarks may help direct these efforts. Hence, we report herein a comprehensive analysis of the thermophysical properties of state-of-the-art ReaxFFs force fields for water. We target ambient (300 K and 0.997 g cm^{-3}) conditions as well as the standard pressure (1 bar), and analyze the performance of these force fields against non-dissociative and non-polarizable empirical force fields that are widely used in the literature.

The structure of this article is as follows. In the next section, we briefly describe the relevant theoretical background of the ReaxFF force field, as well as the simulation details. The simulation results are then presented and analyzed in section III. (1) Standard benchmarks for structure and dynamics: radial distribution functions, atomic charge and dipole moment distributions, vibrational power spectra, and potential energy curves of the water monomer and dimer. (2) Thermodynamic properties: density and thermal expansion coefficient, compressibility, enthalpy of vaporization, surface tension, heat capacity, and the speed of sound. (3) Transport properties: self-diffusion coefficients, shear viscosity and thermal conductivity. Finally, we close the article with a discussion of the overall performance of the ReaxFF models against experiments and compared to state-of-the-art empirical force fields; we provide recommendations on the use of specific ReaxFF force fields based on our benchmarks.

II. METHODOLOGY

This work focuses on structural, dynamic and thermodynamic properties of two ReaxFF water models: water-2017[21] and CHON-2017_weak[23]. ReaxFF employs a bond-order formalism in conjunction with a fluctuating charge description of polarization.[36] A fundamental assumption of ReaxFF is that the bond-order BO_{ij} between atom pairs (i, j) is a function of their interatomic distance r_{ij}, and distinguishes between contributions

$$BO_{ij} = BO_{ij}^\sigma + BO_{ij}^\pi + BO_{ij}^{\pi\pi} \tag{1}$$

from σ-, π-, and double π-bonds. The ReaxFF potential energy E_P^{total} is given by the additive terms

$$E_P^{\text{total}} = E_P^{\text{bond}} + E_P^{\text{val}} + E_P^{\text{tor}} + E_P^{\text{over}} + E_P^{\text{under}}$$
$$+ E_P^{\text{vdW}} + E_P^{\text{Coulomb}} + E_P^{\text{specific}} \tag{2}$$

which are the bond-order dependent energies associated with two-body bonds E_P^{bond}, three-body valence angle strain E_P^{val}, four-body torsional angle strain E_P^{tor}, overcoordination E_P^{over}, and undercoordination E_P^{under}. E_P^{specific} encompasses system-specific contributions. For water these are the lone-pair E_P^{lp} and hydrogen-bonding E_P^{HB} energies, which are also bond-order dependent. The van der Waals, E_P^{vdW}, and Coulomb, E_P^{Coulomb}, energies are given by bond-order independent shielded and tapered pair potentials. Atomic partial charges are assigned on-the-fly using a charge equilibration method, traditionally (and for the RFFs considered in this work) the electronegativity equalization method[37] (EEM),[36,38] although methods such as ACKS2 and eReaxFF have been developed in order to address some of the deficiencies of EEM and extend its range of application.[39] Thus, ReaxFF accounts for polarizability through atomic charge fluctuations. Variations in molecular geometry and interactions with the environment translate into changes in the electrostatic moments.

ReaxFF force fields can be categorised as three-centre, flexible, polarizable, and dissociative within the typical classifications of water models. We additionally benchmark the mSPCFw force field[5] (see Appendix A for details), which models water as a three-site molecule with flexible bonds and H-O-H angle. Hence, it provides a more direct connection with the geometry of the ReaxFF water molecules, while mSPCFw does not explicitly include electronic polarization or bond dissociation. We will also compare the ReaxFF benchmarks with data from the literature for state-of-the-art rigid models, specifically TIP4P/2005.

All statistical uncertainties reported for quantities calculated in this work refer to the standard error of the mean, unless stated otherwise.

A. Simulation Details

We performed both equilibrium and non-equilibrium molecular dynamics (MD) simulations. All simulations were

carried out using the open-source software package LAMMPS (v. 7Aug2019).[38,40] The equations of motion were integrated using the velocity Verlet algorithm and a timestep of $\delta t = 0.2$ fs (unless stated otherwise). 3D periodic boundary conditions were applied in all simulations, except for those of a single molecule in vacuum for which finite (non-periodic) boundary conditions were used. In the ReaxFF charge equilibration procedure, a relative residual norm tolerance of 10^{-6} was used for the employed Preconditioned Conjugate Gradient method.[38]

We note in passing that due to poor energy conservation, it is difficult to perform sufficiently long simulations using ReaxFF force fields in the NVE ensemble. For CHON-2017_weak and water-2017 we observed temperature drifts of (15.1 ± 0.2) K ns^{-1} and (17.2 ± 0.2) K ns^{-1}, corresponding to 0.997 g cm^{-3} and the temperature windows 304-313 K and 297-307 K respectively. The reasons behind this have recently been addressed.[41,42] We therefore relied on the mSPCFw force field to assess the extent to which the employed temperature-control algorithms affected dynamic properties, as compared to the NVE results.

1. Simulations of Bulk Liquid Water

Equilibrium simulations of bulk liquid water were performed in the NVT and NPT ensembles. NVT simulations were carried out at 300 K and the corresponding experimental density of 0.997 g cm^{-3}, while NPT simulations were performed at 1 bar and temperatures ranging from 180-370 K. Temperature was controlled by the Nosé-Hoover chain thermostat, with 3 chains, and a time constant of 0.5 ps. Pressure was controlled with a Nosé-Hoover chain barostat, also with 3 chains, and a time constant of 2 ps. Unless stated otherwise (e.g. for the finite-size analyses) a cubic simulation box containing 521 water molecules was used. For the 521-molecule NVT systems, sampling consisted of 7-10 statistically independent replicas, each equilibrated for 200 ps followed by a 2 ns production run. For the NPT simulations, a single replica was performed for each temperature, with at least 200 ps of equilibration followed by a 10-15 ns production run for the ReaxFF force fields, and 10-20 ns for mSPCFw. Additional details are reported in section III.

For mSPCFw, the electrostatic interactions were handled using the P^{3}M implementation[43] of the Ewald summation method, with a root mean square (RMS) error in per-atom forces of 10^{-6} relative to the force two point charges of elementary charge exert on each other at a distance of 1 Å. A cutoff of 9.8 Å was used for the oxygen-oxygen Lennard-Jones potential, and tail corrections[44] were applied to the total potential energy and pressure.

2. Simulations of the Liquid-Vapour Interface

Direct coexistence simulations of the liquid-vapour interface were carried out in order to calculate the surface tension. An elongated (tetragonal) simulation cell with dimensions $(L_x, L_y, L_z) = (30, 30, 200)$ Å and containing 1024 water molecules stabilised a liquid slab surrounded by vacuum, with two symmetrical interfaces perpendicular to L_z. Simulations were performed in the NVT ensemble at 300 K using the Nosé-Hoover chain thermostat, with 3 chains, and a time constant of 0.5 ps. A single replica was run for each force field, consisting of 200 ps of equilibration followed by 3 ns of production from which data was collected.

For mSPCFw, both electrostatic and dispersion interactions were calculated using the standard 3D Ewald summation method, with a relative RMS per-atom force error of 10^{-6}. The long-range dispersion interactions are required to obtain coexistence densities consistent with the densities obtained using NPT simulations that include tail corrections for the Lennard-Jones potential.

3. Non-Equilibrium Molecular Dynamics Simulations

Boundary-driven non-equilibrium molecular dynamics (NEMD) simulations were used to model water in the stationary state, and thereby calculate the thermal conductivity. An elongated (tetragonal) simulation cell of dimensions $L_x = L_y = 25$ Å was used, while L_z was varied to investigate finite-size effects (see section III M). In all cases the number of molecules was chosen to give an average density of $\rho_{\text{box}} = 0.997$ g cm^{-3}. Two thermostatting regions, hot and cold, of width 5 Å were located in the centre and edges of the box, respectively (see Fig. 15). The thermostatting regions extended in the (x, y) plane such that the temperature gradients were generated along the z-direction. A Langevin thermostat with a damping parameter of 20 fs was applied to all atoms within these regions, while the trajectories of all other atoms were evolved using standard Newtonian dynamics. The system's centre-of-mass velocity was subtracted from each atom at every timestep in order to ensure good linear momentum conservation. In the stationary state, this setup results in two equal but opposite temperature gradients, such that the system is completely periodic. The heat flux across the system, $J_q = (0, 0, \pm J_q)$, can be obtained from the continuity equation

$$J_q = \frac{|\langle \Delta U \rangle|}{2\delta t A} \qquad (3)$$

where $A = L_x \times L_y$ is the cross-sectional area of the simulation box, δt is the timestep, and ΔU is the internal energy exchanged at each timestep, between each thermostatting region and its thermal reservoir. The factor of 2 in the denominator accounts for the two heat fluxes (equal magnitude and opposite direction) generated in this setup.

To ensure adequate sampling, 10 statistically independent replicas were run for each set of simulation conditions. Each replica consisted of at least an initial 200 ps to establish the stationary state, followed by trajectories spanning 1-2 ns for data collection.

For mSPCFw, the electrostatic interactions were handled using the P^{3}M method[43], again with a relative RMS per-atom force error of 10^{-6}. A cutoff of 9.8 Å was used for the oxygen-oxygen Lennard-Jones potential.

III. RESULTS & DISCUSSION

A. Radial Distribution Functions

Radial distribution functions (RDFs), $g(r)$, were calculated using a bin width of 0.01 Å. Coordination numbers n were calculated based on the $g(r)$ definition according to

$$n(R_c) = 4\pi\rho_N \int_0^{R_c} r^2 g(r)dr \qquad (4)$$

where r is the radial distance, ρ_N is the number density of the coordinating species, and R_c is the radial cutoff distance. Oxygen-oxygen $g_{OO}(r_{OO})$, oxygen-hydrogen $g_{OH}(r_{OH})$ and hydrogen-hydrogen $g_{HH}(r_{HH})$ RDFs are shown in Fig. 1, and numerical values for the first maxima/minima are reported in Table. I. The O-O RDF is a primary figure of merit for the structure of water models. While nuclear quantum effects (NQEs) soften the first peaks of g_{OO}, g_{OH} and g_{HH},[60,61] the g_{OO} is much less affected by NQEs, and therefore provides a fairer comparison for simulations with classical nuclear dynamics.

Regarding the experimental reference, there has been controversy about the height of the first peak (see literature cited in Ref. 46), but the high-energy x-ray diffraction measurements[46] we compare to are generally accepted to supersede earlier work. Compared to our simulations these measurements correspond to slightly different thermodynamic conditions, 295 K and ambient pressure, while the experimental reference for g_{OH} and g_{HH} from neutron diffraction measurements[62] correspond to 298 K and 1 bar. We additionally show the g_{OO} from Ref. 62, noting that the qualitative comparisons to the shape of the first peak do not change. More recent x-ray measurements[63-65] extend the temperature range examined, and report ambient condition O-O RDFs in very good agreement with Ref. 46.

The CHON-2017_weak O-O RDF features a broader peak and underestimated first maximum $g_{OO}^{max,1}$. In contrast, the water-2017 O-O RDF possesses a narrower peak, and an overestimated $g_{OO}^{max,1}$. Although slightly overestimated, CHON-2017_weak has a peak position $r_{OO}^{max,1} = (2.85 \pm 0.03)$ Å in better agreement with the experimental value of (2.80 ± 0.01) Å than water-2017, which underestimates the position of the first maximum with $r_{OO}^{max,1} = (2.68 \pm 0.01)$ Å. Likewise, CHON-2017_weak better predicts the position of the first minimum $r_{OO}^{min,1}$, but the depth of the minimum is exaggerated. water-2017 better reproduces the first minimum, but slightly overestimates $r_{OO}^{min,1}$. Both RFFs accurately reproduce the second peak, which is characteristic of tetrahedral order.

Classical force fields, including TIP4P/2005, SPC/E and mSPCFw (this work), typically underestimate $r_{OO}^{max,1}$ and overestimate $g_{OO}^{max,1}$, while the longer range structure is more accurately reproduced (although TIP4P/2005 underestimates the position of the second peak $r_{OO}^{max,2}$ by ~ 0.6 Å at 300 K and 1 bar).[66] However, with $g_{OO}^{max,1} = (3.62 \pm 0.02)$ Å, the overstructuring of the first maximum exhibited by water-2017 is more severe. DFT descriptions beyond GGA functionals (e.g.
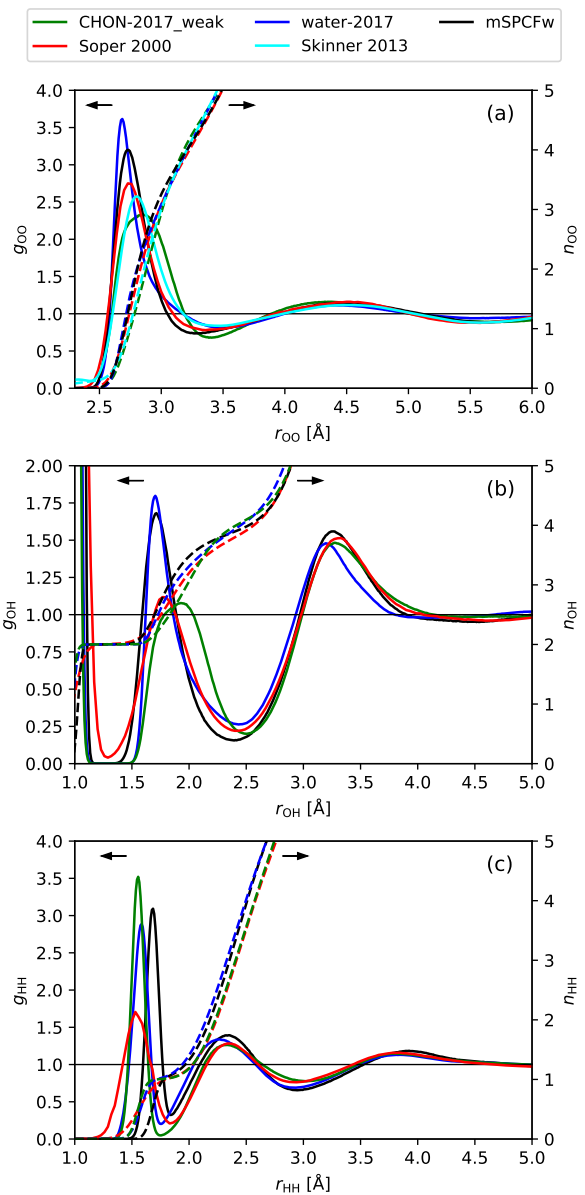

FIG. 1. Radial distribution functions (RDFs) of liquid water at 300 K and 0.997 g cm^{-3} as predicted by the CHON-2017_weak and water-2017 ReaxFF models, as well as the mSPCFw force field. (a) Oxygen-oxygen RDFs g_{OO} and coordination numbers n_{OO}. (b) Oxygen-hydrogen RDFs g_{OH} and coordination numbers n_{OH}. (c) Hydrogen-hydrogen RDFs g_{HH} and coordination numbers n_{HH}. $r_{\alpha\beta}$ is the radial distance between species α and β. In all cases, the solid lines denote the RDFs (left axes), while the dashed lines denote the coordination numbers (right axes). Experimental RDFs are taken from Refs. 46,62

meta-GGAs, hybrid functionals, possibly with dispersion corrections and accounting for NQEs)[14,16,18,67] and many-body potentials, for example MB-pol[66,68], can offer more accurate predictions of the first O-O RDF peak at ambient temperatures than the RFFs and classical models.

Both RFFs are in relatively good agreement with the ex-

TABLE I. Thermphysical properties of water at 300 K and 0.997 g cm^{-3}, as predicted by ReaxFF and mSPCFw force fields. Symbol meanings are given in the main text. Parentheses contain the statistical uncertainties or estimated errors in the least significant figure.

	CHON-2017_weak	water-2017	mSPCFw	Experiment
P [bar]	138(3)	−178(3)	−214(2)	11 [a]
$\langle r_{\mathrm{OH}}^{\mathrm{bond}} \rangle$ [Å]	0.981(1)	0.989(1)	1.034(1)	-
$\langle \theta_{\mathrm{HOH}}^{\mathrm{angle}} \rangle$ [°]	105.2(1)	105.7(1)	109.1(1)	-
$r_{\mathrm{OO}}^{\mathrm{max,1}}$ [Å], $g_{\mathrm{OO}}^{\mathrm{max,1}}$, $n_{\mathrm{OO}}^{\mathrm{max,1}}$	2.85(3), 2.33(1), 1.8(2)	2.68(1), 3.62(2), 0.9(1)	2.73(1), 3.20(2), 1.26(8)	2.80(1), 2.57(5), 1.48(7) [b]
$r_{\mathrm{OO}}^{\mathrm{min,1}}$ [Å], $g_{\mathrm{OO}}^{\mathrm{min,1}}$, $n_{\mathrm{OO}}^{\mathrm{min,1}}$	3.39(1), 0.681(3), 4.7(1)	3.49(2), 0.813(2), 5.1(1)	3.27(2), 0.738(2), 4.2(1)	3.45(4), 0.84(2), 5.0(2) [b]
$n_{\mathrm{OO}}(r_{\mathrm{OO}} = 3.30 \text{ Å})$	4.44(1)	4.36(1)	4.30(1)	4.3(1) [b]
$(\langle q_{\mathrm{O}} \rangle, \sigma(q_{\mathrm{O}}))$ [e]	−0.7122(2), 0.0210(4)	−0.7435(2), 0.0250(8)	−0.82, 0	-
$(\langle q_{\mathrm{H}} \rangle, \sigma(q_{\mathrm{H}}))$ [e]	0.3561(1), 0.0203(3)	0.3718(1), 0.0246(5)	0.41, 0	-
$(\langle \mu_{\mathrm{COM}} \rangle, \sigma(\mu_{\mathrm{COM}}))$ [D]	2.0382(6), 0.1153(9)	2.1322(6), 0.1305(9)	2.3602(6), 0.1382(9)	2.9(6) [c] and 2.95(10) [d]
$(\langle \mu_{\mathrm{GC}} \rangle, \sigma(\mu_{\mathrm{GC}}))$ [D]	2.0386(6), 0.1055(9)	2.1329(6), 0.1165(9)	2.3602(6), 0.1382(9)	-
μ_{rigid} [D]	2.038(3)	2.133(3)	2.361(4)	-
$Q_{T,\mathrm{rigid}}$ [D Å]	1.559(4)	1.667(4)	2.097(5)	-
$\mu_{\mathrm{rigid}}/Q_{T,\mathrm{rigid}}$ [Å^{-1}]	1.307(4)	1.280(3)	1.126(3)	-
$\Delta_{\mathrm{l}}^{\mathrm{g}} \mu$ [D]	−0.370(1) [e(i)], −0.371(1) [e(ii)]	−0.387(1) [e(i)], −0.388(1) [e(ii)]	−0.155(2)	−1.1(1) [f]
O-H stretch, $\tilde{\nu}$ [cm^{-1}]	3000(20), 3260(40)	3170(20), 3390(40)	3420(20)	3404 [g]
H-O-H bend, $\tilde{\nu}$ [cm^{-1}]	1900(20)	1840(20)	1650(10)	1644 [g]
Librations (A$_2$, B$_2$, B$_1$), $\tilde{\nu}$ [cm^{-1}]	440(10)	490(30)	520(30)	400-800 [h] (430, 650, 794) [i]
Intermolecular stretch, $\tilde{\nu}$ [cm^{-1}]	∼120-240 [j]	-	∼140-280 [j]	162 [i], 172-175 [k]
Cage vibrations, $\tilde{\nu}$ [cm^{-1}]	40(10)	40(10)	50(10)	65 [i], 60 [k]
(C_V, C_V^{qc}) [J K^{-1} mol^{-1}]	104.5(9), 68(1)	98(1), 61(1)	111.1(6), 73.8(8)	74.41(7) [l]
C_V^{Δ} [J K^{-1} mol^{-1}], $C_V^{\Delta,\mathrm{intra}}$ [%]	−36.1(4), 68(1)	−37.5(5), 66(1)	−37.3(5), 66(1)	-
D_0 [10^{-5} cm^2 s^{-1}]	2.93(5)	3.64(5)	2.40(3)	2.41(2) [m]
$(\eta_{\mathrm{GK}}, \eta_{\mathrm{YH}})$ [mPa s]	0.70(7), 0.60(9)	0.54(2), 0.50(7)	0.85(1), 0.9(1)	0.854(9) [n]
λ [W K^{-1} m^{-1}]	0.826(4) [o]	0.839(7) [o]	0.873(1) [o]	0.609(4) [p]

[a] IAPWS-95 formulation[45] from the NIST database for 0.99700 g cm^{-3}. Note that the experimental density corresponding to 300 K and 1 bar is 0.997 g cm^{-3} to 3 decimal places.

[b] From Ref. 46, or calculated from the RDF (and associated error) if not provided in text. Corresponds to 295 K and ambient pressure.

[c] From Ref. 47. Corresponds to (297.60 ± 0.05) K and ambient pressure.

[d] From Ref. 48. Corresponds to 300 K. Extracted from experimental refractive index data with the support of classical and *ab initio* simulations.

[e] Using (i) $\langle \mu_{\mathrm{COM}} \rangle$ and (ii) $\langle \mu_{\mathrm{CG}} \rangle$ for the dipole moment of liquid water.

[f] Using the liquid and gas phase dipole moments from Ref. 15 and Refs. 49,50 respectively.

[g] From Refs. 51,52. Corresponds to room temperature and ambient pressure, with measurements in Ref. 52 being carried out at 298 K.

[h] From Refs. 51,53,54 corresponding to room temperature and ambient pressure.

[i] From Ref. 53 corresponding to 297 K and 128 bar.

[j] Shoulder in the oxygen atom power spectrum (see section III C)

[k] From Ref. 54 and works cited therein. Corresponds to room temperature and ambient pressure conditions.

[l] IAPWS-95 formulation[45] from the NIST database. The uncertainties in C_P are ±0.1%. Usually the C_V uncertainties in the liquid region follow from those given for C_P, so uncertainties of ±0.1% have also been assumed. However, owing to the unclear data situation, a more conservative estimate of ±0.75% has also been given in Ref. 45.

[m] From Ref. 55. The stated absolute error limit of ≤ 1% is given in parentheses.

[n] From Ref. 56. Corresponds to 300 K and 1 bar.

[o] The linear response (LR) values corresponding to 300 K and 1.00 g cm^{-3} (see section III M).

[p] From Ref. 57. Corresponds to 300 K and 1 bar. The uncertainty corresponds to the maximum deviation of 0.7% from primary experimental data.

perimental value[46] of $n_{\mathrm{OO}}(R_c/\text{Å} = 3.30) = 4.3 \pm 0.1$, which corresponds to the first minimum in $r_{\mathrm{OO}}^2 g_{\mathrm{OO}}(r_{\mathrm{OO}})$; water-2017 agrees within the associated uncertainties, while CHON-2017_weak slightly overestimates $n_{\mathrm{OO}}(R_c/\text{Å} = 3.30)$. These are inline with popular empirical models which typically give $n_{\mathrm{OO}}(R_c/\text{Å} = 3.30)$ values of 4.3-4.4.[4] The agreement in the coordination numbers shows the local structure is well reproduced by the classical force fields, the main deficiency being the lack of delocalization of water molecules in the hydrogen bonding network, as reflected in the over-structured g_{OO} first maximum. This deficiency can, at least in part,[61] be attributed to NQEs, which are not explicitly accounted for.

The O-H RDF is instructive because its maximum at $r_{\mathrm{OH}} \simeq$ 1.75-1.80 Å directly probes the hydrogen bond between donor H and acceptor O. For CHON-2017_weak the height of this peak is in good agreement with experiment[62], while water-2017 and mSPCFw overestimate the height of the peak by ∼50-60%. The coordination numbers for these three models, the two RFFs and mSPCFw, are very similar (see Fig. 1b), showing that the key difference between CHON-2017_weak and water-2017 is the delocalization of the hydrogen bond structure, reflected in the lower and wider first maximum of CHON-2017_weak. The position of the first intermolecular maximum is slightly overestimated (underestimated) by CHON-2017_weak (water-2017 and SPCFw) with $r_{\mathrm{OH}} \simeq$ 1.94 Å ($r_{\mathrm{OH}} \simeq$ 1.70-1.72 Å), indicative of a longer (shorter) and therefore weaker (stronger) hydrogen bond. Overall these results indicate that CHON-2017_weak predicts weaker hydrogen bonding. Advancing the discussion below, we will see that this is reflected in the enthalpy of vaporization, which is

TABLE II. Thermodynamic properties of water at standard pressure, as predicted by ReaxFF water and mSPCFw force fields. All properties correspond to 300 K and/or 1 bar, except for coexistence properties (ΔH_{vap} and γ) which correspond to the vapour pressure at 300 K. Symbol meanings are given in the main text. Parentheses contain the statistical uncertainties or estimated errors in the least significant figure.

	CHON-2017_weak	water-2017	mSPCFw	Experiment
ρ [g cm^{-3}]	0.9921(2)	1.0032(1)	1.0067(1)	0.9966 [a]
α_P [10^{-4} K^{-1}]	2.0(2)	3.3(2)	4.4(1)	2.7 [b]
T_{MD} [K]	255(3)	205(6)	252(3)	277 [b]
ΔH_{vap} [kJ mol^{-1}]	49.27(5)	52.09(6)	52.49(6)	43.908(7) [c]
γ [mN m^{-1}]	67(2)	59(1)	63(1)	71.7(4) [d]
β_T [Mbar^{-1}]	38.2(3)	31.8(1)	42.5(2)	45.1 [b]
$T_{\beta_T,\text{min}}$ [K]	260(40)	None	None	319 [b]
(C_P, C_P^{qc}) [J K^{-1} mol^{-1}]	106(1), 70(2)	100.9(6), 63(1)	115(1), 78(2)	75.32(8) [e]
(C_V, C_V^{qc}) [J K^{-1} mol^{-1}]	105(1), 69(2)	99.0(7), 62(1)	113(1), 75(2)	74.41(7) [e]
C_V^{Δ} [J K^{-1} mol^{-1}], $C_V^{\Delta,\text{intra}}$ [%]	−36.0(5), 68(1)	−37.4(5), 66(1)	−37.3(4), 66(1)	-
$\gamma_0, \gamma_0^{\text{qc}}$	1.006(1), 1.008(2)	1.019(2), 1.031(3)	1.022(1), 1.032(1)	1.012(1) [e]
$(T_{C_P,\text{min}}, T_{C_P^{\text{qc}},\text{min}})$ [K]	None, None	270(30), None [f]	None, None	310(10) [e]
(c_S, c_S^{qc}) [m s^{-1}]	1629(7), 1632(7)	1789(4), 1799(4)	1551(4), 1559(4)	1501.5 [g]
$(T_{c_S,\text{max}}, T_{c_S^{\text{qc}},\text{max}})$ [K]	260(40), 260(40)	None, None	None	347 [b]

[a] IAPWS-95 formulation[45] from the NIST database. Uncertainty of ±0.0001%.

[b] Determined from the IAPWS-95 formulation from the NIST database. The associated uncertainty is less than the stated level of precision.

[c] IAPWS-95 formulation[45] from the NIST database. Uncertainty from Ref. 58.

[d] From Ref. 59. Uncertainties are estimated based on the reliability of the experimental data.

[e] IAPWS-95 formulation[45] from the NIST database. The uncertainties in C_P are ±0.1%. Usually the C_V uncertainties in the liquid region follow from those given for C_P, so uncertainties of ±0.1% have also been assumed. However, owing to the unclear data situation, a more conservative estimate of ±0.75% has also been given in Ref. 45.

[f] Or moved to a lower temperature: $T_{C_P,\text{min}} > T_{C_P^{\text{qc}},\text{min}}$.

[g] IAPWS-95 formulation[45] from the NIST database. Uncertainty of ±0.005%.

also lower for CHON-2017_weak.

The H-H RDFs show different trends. In this instance, the position of the first maximum is very similar for both RFFs, and lower than the mSPCFw prediction since the RFFs have shorter average bond lengths $\langle r_{\text{OH}}^{\text{bond}} \rangle$ and smaller average bond angles $\langle \theta_{\text{HOH}}^{\text{angle}} \rangle$ (see Table I). Beyond the intramolecular peak ($r_{\text{HH}} \simeq$ 1.5-1.7 Å) the intermolecular long-range structure ($r_{\text{HH}} > 2$ Å) agrees reasonably well with the experiments for all the models, both in phase and height of the maxima/minima.

We note that the water-2017 RDFs reported herein are consistent with Ref. 34, while those in Ref. 21 are in better agreement with experiment. We are able to reproduce the RDFs in Ref. 21 using a bin width of 0.1 Å, and therefore attribute this discrepancy to the different bin width employed in our work (0.01 Å), which results in the better resolution of the RDF maxima.

B. Atomic Charges and Electrostatic Moments

In EEM, atomic partial charges are assigned on-the-fly with the view of minimizing the total electrostatic energy of the system under constraints of net system charge.[37,38] The atomic charge distributions of the ReaxFF water models at 300 K and 0.997 g cm^{-3} are shown in Fig. 2; averages and

standard deviations are given in Table I. Both RFFs predict atomic charges with smaller magnitudes compared to the classical mSPCFw model, and indeed all models in the SPC family (SPC, SPCE, SPCFw, SPCFd), which are arguably the most successful (certainly the most popular) 3-site models of water. In 3-site models, partial charges are assigned to each atom, making them the most suitable for comparison to the RFFs.

In our simulations, the global charge neutrality constraint in EEM ensures that the whole system has a net-zero charge,[38] but no such condition is imposed on individual molecules. Consequently, we observe molecule charge distributions centred on zero, but with non-zero standard deviations of (0.0378 ± 0.0008) e and (0.0452 ± 0.0008) e for CHON-2017_weak and water-2017 respectively. Only the lowest-order non-zero electric multipole moment of a charge distribution is translationally invariant. For ReaxFF water molecules this is the total charge, and dipole moments are therefore origin dependent. In order to gauge the sensitivity of molecular dipole moment on the choice of origin, we compare the dipole moments defined relative to the centre of mass μ_{COM} and centre of geometry μ_{GC}. These dipole distributions are shown in Fig. 2c, and are characterised by means that differ by only $\sim 10^{-3} - 10^{-4}$ D due to the choice of origin. However, standard deviations differ more appreciably, by $\sim 10^{-2}$ D. The instantaneous differences $\mu_{\text{COM}} - \mu_{\text{GC}}$ (Fig. 2d) are slightly more significant, with $\langle |\mu_{\text{COM}} - \mu_{\text{GC}}| \rangle = (0.0479 \pm 0.0008)$ D and $\langle |\mu_{\text{COM}} -$
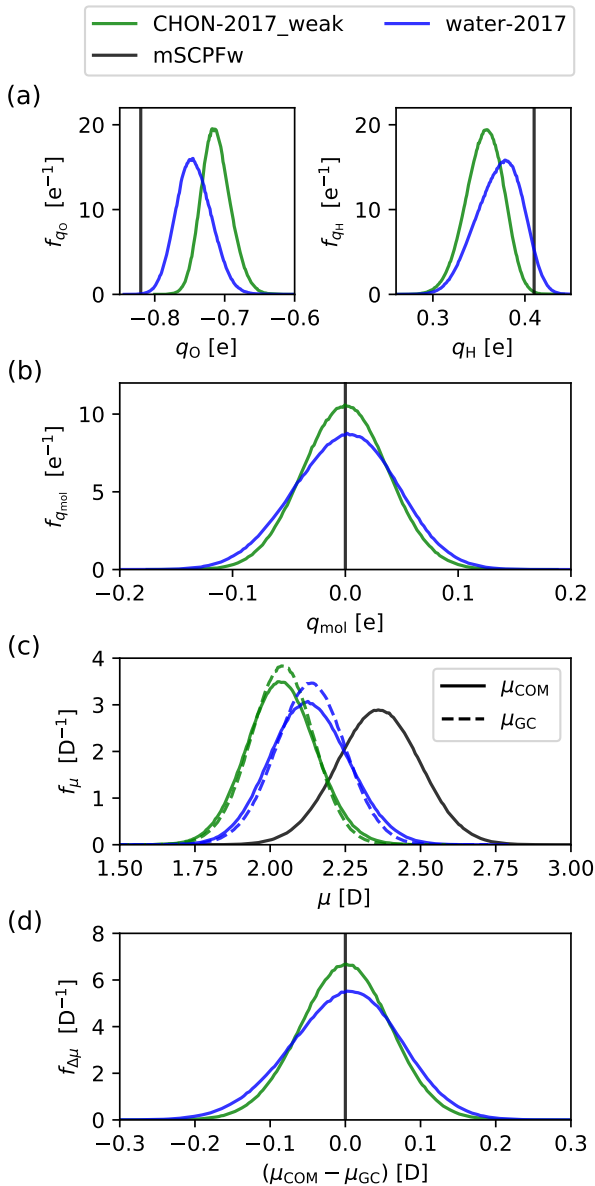
FIG. 2. Atomic charge and molecular multipole moment probability density functions f_X (where X is the variable) for liquid water at 300 K and 0.997 g cm^{-3} as predicted by the CHON-2017_weak and water-2017 ReaxFF models, as well as the mSCPFw force field: (a) oxygen (left) and hydrogen (right) atomic charges q_O and q_H respectively; (b) total molecular charge q_{mol}; (c) molecular dipole moment μ as measured relative to the centre of mass, μ_{COM}, and centre of geometry, μ_{GC}; and (d) the instantaneous difference $\Delta\mu = \mu_{COM} - \mu_{GC}$.

$\mu_{GC}|\rangle = (0.0578 \pm 0.0008)$ D for CHON-2017_weak and water-2017 respectively.

For both RFFs, the smaller atomic charges translate into smaller average dipole moments of $\sim$2.04 D and $\sim$2.13 D for CHON-2017_weak and water-2017 respectively, which are underestimated compared to the experimental value[47,48] of $\sim$2.95 D, but of the same order as the dipole moment of cen-

tral force models[7]. The mSPCFw dipole moment of $\sim$2.36 D is also underestimated compared to experiment, and is similar to the dipole of state-of-the-art 4-site models, namely TIP4P/2005 and OPC (see Table III). The atomic charges and dipole moments along the 1 bar isobar are shown in Fig. 3. For the dipole (atomic charge) distributions, average magnitudes increase (decrease) with temperature. The standard deviations increase with temperature, with $\sigma(\mu_{COM}) > \sigma(\mu_{GC})$ for the dipole moment.

The multipole moments of water are crucial for building accurate water models. For non-polarizable rigid models $2.4 \leq \mu/D \leq 2.6$ and $2.2 \leq Q_T/(D \text{ Å}) \leq 2.4$ have been shown to produce the highest quality models for liquid water,[70] and a $\mu/Q_T \sim 1.0$ Å^{-1} ratio is particularly important for reproducing the phase diagram of water, specifically the right order of stability for the phases of ice.[71,72] $Q_T = (Q_{xx} - Q_{yy})/2$ is a convenient measurement of the quadrupole moment; it is an origin-independent scalar in the frame of reference where the z-axis bisects the H-O-H angle and the x-axis is parallel to the line joining the two hydrogen atoms. The reduction of the quadrupole moment tensor to Q_T relies on the C_{2v} symmetry imposed at all times by rigid models, but not by flexible and/or polarizable models. For the flexible models at finite temperature, we therefore calculate $Q_{T,\text{rigid}}$, and additionally μ_{rigid}, as if the molecules were rigid, using the average bond length, bond angle and atomic partial charges obtained from the MD simulations. This approach assumes that the charge and geometry contributions to the multipole moments are decoupled, and that fluctuations from the average values do not have a significant impact. In the liquid phase (Table I) μ_{rigid} agrees with the MD estimates to within their associated uncertainties, while differences $\sim 10^{-2}$-10^{-3} D are observed for the RFF water molecules in vacuum (Table III), indicating that these are good approximations. At 300 K and 0.997 g cm^{-3}, the RFFs have much lower quadrupole moments of $Q_T \approx 1.5$-1.6 D Å, and greater ratios $\mu/Q_T \approx 1.3$ Å^{-1}, while mSPCFw has values inline with popular rigid force fields.

The RFFs and mSPCFw are able to model the shift in dipole moment $\Delta_l^g\mu$ when going from the liquid to vapour phase. At 300 K, and approximating the vapour phase by a water molecule in vacuum, we obtain $\Delta_l^g\mu$ values between -0.37 D and -0.39 D for the RFFs, and a smaller $\Delta_l^g\mu \approx -0.16$ D for mSPCFw. In the latter case the change is solely due to the modification of molecular geometry, while for the RFFs we decompose $\Delta_l^g\mu$ into contributions from the change in atomic charge and the change in molecular geometry, again using the average charges and geometries given in Table I and Table III. For both RFFs, the majority of $\Delta_l^g\mu$ originates from the charge contribution: 88-90% for CHON-2017_weak and 92-93% for water-2017. The dipole moment of a water molecule in vacuum has been experimentally determined to be 1.855 D.[49,50] CHON-2017_weak and water-2017 underestimate this value by 10% and 6% respectively, while in contrast mSPCFw overestimates it by 18%. All three force fields greatly underestimate the shift in dipole moment of $\Delta_l^g\mu \sim -1.1$ D expected from experiment[47–50].

Comparing to DFT, many functionals of varying levels of theory (semi-local, van der Waals and hybrid functionals) are
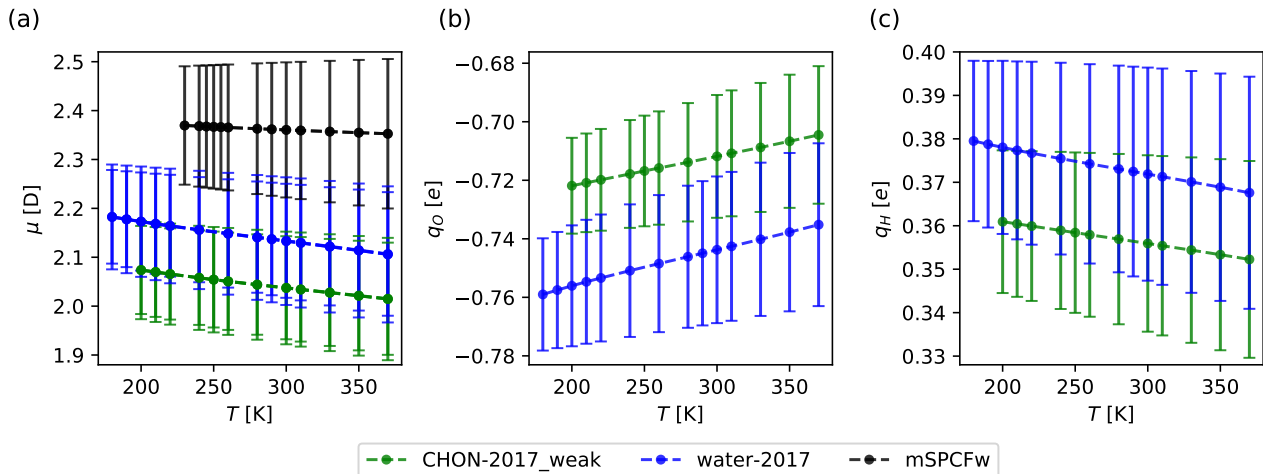
FIG. 3. (a) Molecular dipole moments μ, (b) oxygen atomic charges, and (c) hydrogen atomic charges of liquid water at temperatures T along the 1 bar isobar, as predicted by the CHON-2017_weak and water-2017 ReaxFF models, as well as the mSPCFw force field. In all cases the error bars represent the standard deviation σ. In (a), both $\sigma(\mu_{\mathrm{COM}})$ and $\sigma(\mu_{\mathrm{GC}})$ are shown with $\sigma(\mu_{\mathrm{COM}}) > \sigma(\mu_{\mathrm{GC}})$, while $\langle\mu_{\mathrm{GC}}\rangle$ and $\langle\mu_{\mathrm{GC}}\rangle$ cannot be distinguished on the scale of the plot.

TABLE III. Molecular geometry and multipole moments of a water molecule in vacuum for selected force fields. $r_{\mathrm{OH}}^{\mathrm{bond}}$ and $\theta_{\mathrm{HOH}}^{\mathrm{angle}}$ are the O-H bond length and H-O-H bond angle respectively; q_{H} is the atomic partial charge for hydrogen; μ and Q_T are the dipole and quadrupole moment respectively. Statistical uncertainties in the least significant figure are given in parentheses.

Model	$r_{\mathrm{OH}}^{\mathrm{bond}}$ [Å]	$\theta_{\mathrm{HOH}}^{\mathrm{angle}}$ [°]	q_{H} [e]	μ [D]	Q_T [D Å]	μ/Q_T [Å^{-1}]
CHON-2017_weak	0.953[a], 0.956(1)[b]	104.14[a], 104.8(1)[b]	0.2989[a], 0.2986(1)[b]	1.6824[a], 1.668(1)[b], 1.674(3)[c]	1.2170[a], 1.233(3)[c]	1.3824[a], 1.357(4)[c]
water-2017	0.950[a], 0.954(1)[b]	103.16[a], 103.8(1)[b]	0.3108[a], 0.3102(1)[b]	1.7631[a], 1.745(1)[b], 1.754(3)[c]	1.2413[a], 1.261(3)[c]	1.4203[a], 1.391(4)[c]
mSPCFw	1.012[a], 1.015(1)[b]	113.24[a], 113.1(1)[a]	0.41	2.1930[a], 2.205(2)[b], 2.201(4)[c]	2.1095[a], 2.118(5)[c]	1.0396[a], 1.039(3)[c]
SPC/E	1.0	109.47	0.4238	2.3505	2.0356	1.1547
TIP4P/2005	0.9572, 0.1546[d]	104.52	0.5564	2.3052	2.2969	1.0036
OPC	0.8724, 0.1594[d]	103.6	0.6791	2.4797	2.2997	1.0782
Experiment[49,50,69]	-	-	-	1.855	2.56(1)	0.723(4)

[a] Geometrically optimised molecules (0 K).
[b] Average (mean) at 300 K. The canonical distribution was sampled using the Nosé-Hoover chain thermostat, with 3 chains, and a time constant of 0.5 ps.
[c] Calculated using the average molecular geometry and atomic partial charges at 300 K.
[d] The distance r_{OM} between the oxygen atom and the massless M site that carries the negative charge in these 4-site models. M is coplanar with the O and H sites and bisects the H-O-H angle.

able to reproduce the experimental dipole moment of a water molecule in vacuum to within 3%.[73] Estimates of the liquid phase dipole moment, using maximally localized Wannier functions to spatially partition electron density, typically range from 2.8-3.3 D depending on the functional,[73,74] with the SCAN functional giving[74] (2.94 ± 0.28) D at 330 K (an elevated temperature was used to crudely[18] approximate NQEs) in good agreement with experimental[47,48] values. Thus, despite being parameterized primarily using DFT data, the RFFs predict dipole moments much less accurately. Indeed, the first generation ReaxFF water model (on which CHON-2017_weak and water-2017 are based) used Mulliken charges as target parameters, although a relatively low weight was placed on these. Although still widely used, the Mulliken population analysis is (among other problems) extremely sensitive to basis set choice, and care must be taken to ensure

the obtained partial charges are chemically meaningful. For this reason, Mulliken charges for a single water molecule have been shown to be unreliable, irrespective of the electronic structure method used.[75,76] Recent benchmarks have shown that the Mulliken population analysis performs relatively poorly compared to other charge partitioning schemes for the assignment of atomic partial charges and dipole moments in water systems including the isolated water molecule, dimer, and clusters.[76]

C. Vibrational Power Spectrum

The unambiguous assignment of spectral features to the molecular-scale dynamics of liquid water remains a challenge due to the fluctuating nature of the hydrogen bonding net-

TABLE IV. Normal mode frequencies of a water molecule in vacuum for selected force fields. $\tilde{\nu}_1$, $\tilde{\nu}_2$ and $\tilde{\nu}_3$ denote the wavenumbers of the symmetric stretch, bend and asymmetric stretch respectively.

Model	$\tilde{\nu}_1$ [cm^{-1}]	$\tilde{\nu}_2$ [cm^{-1}]	$\tilde{\nu}_3$ [cm^{-1}]	$(\tilde{\nu}_3 - \tilde{\nu}_1)$ [cm^{-1}]
CHON-2017_weak	3128	1783	3356	228
water-2017	3331	1576	3487	156
mSPCFw	3649	1584	3734	85
Experiment[83]	3657	1594	3756	99

work in which hydrogen bonds are continually broken and reformed, and the presence of both intra- and intermolecular couplings between vibrational modes.[77–80] In order to probe key dynamics, we calculate the vibrational power spectrum from the Fourier transform of the velocity autocorrelation function (VACF) of all atoms,

$$I(\nu) \propto \lim_{\tau \to \infty} \int_{-\tau}^{\tau} \langle \boldsymbol{v}_j(t_0 + t) \cdot \boldsymbol{v}_j(t_0) \rangle e^{-i2\pi\nu t} dt \qquad (5)$$

where I is the intensity, ν is the vibrational frequency, $\boldsymbol{v}_j$ is the velocity of atom j, and t is the elapsed time from arbitrary starting time t_0. The power spectrum allows an investigation of vibrational frequencies independently of infrared (IR) and Raman selection rules, while the calculation of these spectra would be required for direct comparisons with experiment.[81] We additionally calculate the vibrational frequencies of a single water molecule in vacuum (Table IV) from the eigenvalues of the dynamical matrix. The dynamical matrices (mass-weighted Hessians) of the geometrically optimised molecules were calculated using the finite-difference method, using a displacement of 10^{-4} Å.

The power spectra at 300 K and 0.997 g cm^{-3} are shown in Fig. 4, and the peak positions are given in Table I. The IR spectrum of liquid water at ambient conditions features a broad and asymmetric O-H stretching peak at $\sim$3400 cm^{-1}. The RFFs possess red-shifted stretching regions, and do not reproduce the single peak: CHON-2017_weak predicts two distinct maxima, while water-2017 predicts two maxima and a shoulder. This peak splitting has previously been observed for CHON-2017_weak, and was attributed to the large difference between gas phase symmetric ν_1 and asymmetric ν_3 stretching frequencies.[25] We also find this to be the case, with CHON-2017_weak and water-2017 yielding differences of 228 cm^{-1} and 156 cm^{-1} respectively, compared to 99 cm^{-1} from experiment. mSPCFw predicts $\tilde{\nu}_1 - \tilde{\nu}_3 = 85$ cm^{-1} in better agreement with experiment, and reproduces the single O-H stretching peak in its liquid power spectrum. Indeed, classical force fields that employ Morse potentials for the O-H bond, such as mSPCFw and TIP4P/2005f, feature this single peak, while harmonic potentials neglect bond anharmonicity and often lead to peak splitting. This peak splitting has been also observed in central force type models.[7]. The introduction of anharmonicity results in an additional red-shift in the stretching modes, and eventually a single stretching peak[82]. Additionally, both RFFs possess a H-O-H bending frequency blue-shifted relative to experiment: by ~ 260 cm^{-1} for CHON-2017_weak and ~ 200 cm^{-1} for water-2017.

Red-shifts in the O-H stretching frequency and blue-shifts

in the H-O-H bending frequency are positively correlated with the strength of the H$_2$O-HOH hydrogen bond.[77,80,84–86] Comparing the frequency shifts moving from vacuum to the liquid phase for CHON-2017_weak, water-2017 and mSPCFw, the O-H stretching (H-O-H bending) frequencies are red-shifted (blue-shifted) upon hydration by $\sim$110 cm^{-1} ($\sim$120 cm^{-1}), $\sim$130 cm^{-1} ($\sim$260 cm^{-1}) and $\sim$270 cm^{-1} ($\sim$70 cm^{-1}) respectively. The experimental red-shift (blue-shift) in stretching (bending) frequency is $\sim$ 300 cm^{-1} ($\sim$ 50 cm^{-1}). Both RFFs underestimate (overestimate) the shift in stretching (bending) frequency, while mSPCFw predicts shifts in good agreement with experiment. The RFFs predict gas phase stretching frequencies $\sim$270-530 cm^{-1} lower than experiment, and the CHON-2017_weak ν_2 bend is additionally blue-shifted by $\sim$ 190 cm^{-1}. It is therefore impossible for the RFFs investigated here to predict both accurate liquid phase frequencies and shifts from the gas phase.

The vibrational spectra of liquid water feature a broad band spanning 400-800 cm^{-1} corresponding to the three libration modes;[51,53,54] this is reproduced by the RFFs, as well as mSPCFw and TIP4P/2005f[87], which all predict a maximum located between the experimental A$_2$ and B$_2$ mode peaks[53,54] (as determined[53] by Guassian deconvolution). Intermolecular stretching is not observed as a peak in the power spectrum for both the RFFs and mSPCFw. However, a shoulder centred around 200 cm^{-1} is observed in the oxygen atom power spectrum $I_O(\nu)$ (Fig. 5) for CHON-2017_weak and mSPCFw, but not for water-2017, indicating[88] the presence of this O-O stretch along the H-bond direction. Interestingly, TIP4P/2005f does display this peak in the power spectrum of hydrogen velocities relative to oxygen velocities, albeit at a slightly higher frequency of 230 cm^{-1}.[87] Both RFFs, as well as mSPCFw and TIP4P/2005f[87], have a peak $\sim$40-50 cm^{-1} corresponding to cage vibrations[88], close to the Raman peak[53,54] near 60 cm^{-1}.

D. Potential Energy Curves of the Water Monomer & Dimer

The ReaxFF force field parameterization procedure included fitting various potential energy curves (PECs) to those predicted by quantum-mechanical methods.[20,21,23] In Fig. 6 we compare the PECs predicted by the RFFs and mSPCFw, for bond dissociation and angle strain in the isolated water molecule, and hydrogen bonding in the water dimer.

For the intramolecular PECs, only the single oxygen-hydrogen distance r_{OH} or H-O-H angle θ_{HOH}^{angle} parameter was varied; all other degrees of freedom were constrained to the values of the minimum-energy geometry, which has potential energy E_P^{min}. The O-H bond dissociation energy D_0^{bond} of both RFFs are in good agreement with the experimental value[89] of 492.21 kJ mol^{-1} for H$_2$O^{16} (which includes NQEs); with values (percent errors) of 465.60 kJ mol^{-1} (-5%) and 497.52 kJ mol^{-1} (1%) for CHON-2017_weak and water-2017 respectively, CHON-2017_weak slightly underestimates D_0^{bond}. mSPCFw reproduces the experimental D_0^{bond} because it was parameterized to do so (see Appendix A).

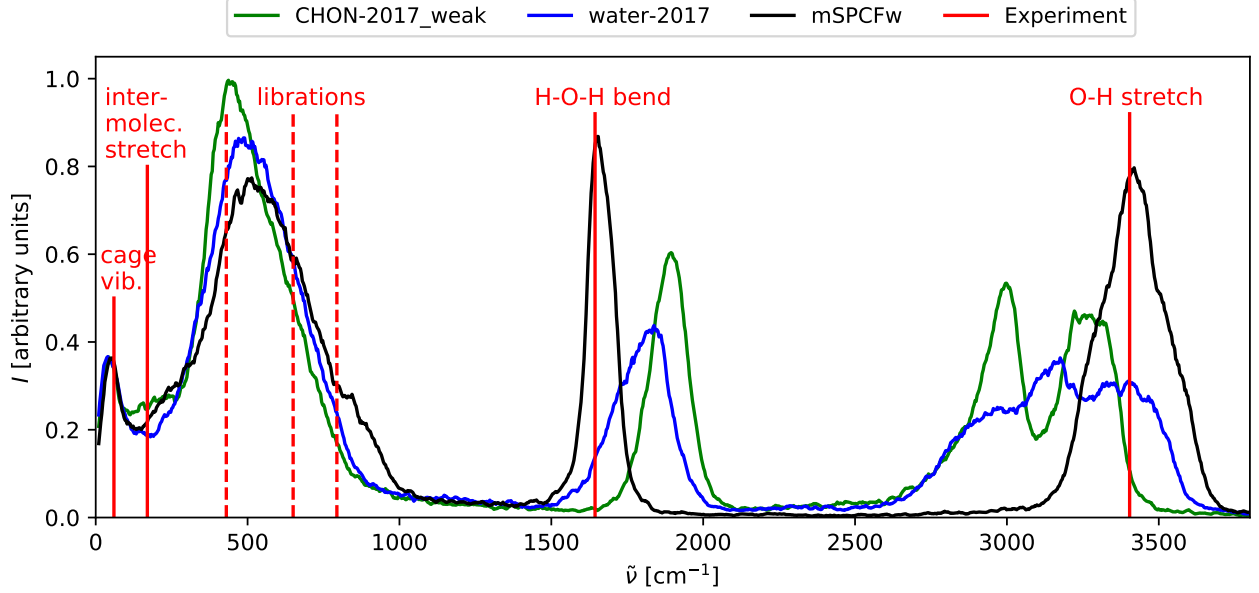The insets in Fig. 6 show the intramolecular PECs close

FIG. 4. Vibrational power spectrum of liquid water at 300 K and 0.997 g cm^{-3} as predicted by the CHON-2017_weak and water-2017 ReaxFF water models, as well as the mSPCFw force field. I is the intensity at wavenumber $\tilde{\nu}$. Power spectra share the same normalization condition $\int_0^\infty I(\tilde{\nu})d\tilde{\nu} = C$, where C is a constant. Experimental lines are from Refs. 51–54.
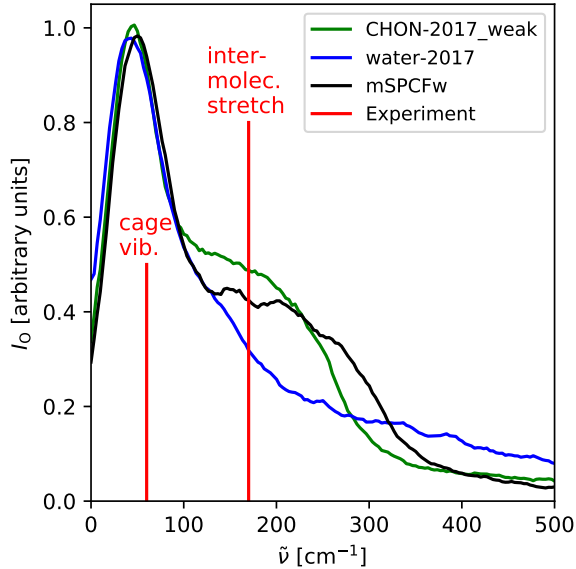

FIG. 5. Oxygen atom power spectra of liquid water at 300 K and 0.997 g cm^{-3} as predicted by the CHON-2017_weak and water-2017 ReaxFF water models, as well as the mSPCFw force field. I_O is the intensity at wavenumber $\tilde{\nu}$. Power spectra share the same normalization condition $\int_0^\infty I_O(\tilde{\nu})d\tilde{\nu} = C$, where C is a constant. Experimental lines are from Refs. 53,54.

to their minima, where the harmonic approximation is valid. Fitting harmonic potentials of the form $E_P(r_{OH}) - E_P^{min} = k_b(r_{OH} - r_0)^2/2$ to the region $r_0 \pm 0.01$ Å gives O-H bond

force constants $k_b/(\text{kJ mol}^{-1} \text{ Å}^{-2})$ of 3472, 3807 and 4585 for CHON-2017_weak, water-2017 and mSPCFw, respectively. The RFF force constants are smaller the ~ 4400 kJ mol^{-1} Å^{-2} typically employed in classical models with harmonic bonds,[4,90,91] and the fitted k_b for mSPCFw. Similarly, fitting harmonic potentials $E_P(\theta_{HOH}^{angle}) - E_P^{min} = k_a(\theta_{HOH}^{angle} - \theta_0)^2/2$ to the region $\theta_0 \pm 0.5$ ° gives $k_a/(\text{kJ mol}^{-1} \text{ rad}^{-2})$ of 480 and 367 for CHON-2017_weak and water-2017, respectively. These RFF force constants k_a are comparable to the $\sim$300-400 kJ mol^{-1} rad^{-2} typically[4,5,87] used in classical models ($k_a \approx 424$ kJ mol^{-1} rad^{-2} for mSPCFw – see Appendix A). Further reductions in the regions used to fit the force constants may lead to changes on the order of 10^0-10^1 kJ mol^{-1} Å^{-2} for k_b and 10^0 kJ mol^{-1} rad^{-2} for k_a. The force constants are consistent with the order of stretching ($\tilde{\nu}$(mSPCFw) > $\tilde{\nu}$(water-2017) > $\tilde{\nu}$(CHON-2017_weak)) and bending ($\tilde{\nu}_2$(CHON-2017_weak) > $\tilde{\nu}_2$(mSPCFw) > $\tilde{\nu}_2$(water-2017)) normal mode frequencies, as given in table IV.

The water dimer interaction energy $E_P^{int} = E_P^{min}((H_2O)_2) - 2E_P^{min}(H_2O)$ as a function of oxygen-oxygen distance r_{OO}, for each force field, is shown in Fig. 6(c). Only the distance r_{OO} was constrained, and each configuration was geometrically optimized. This cut through the potential energy surface corresponds to a hydrogen-bonded structure of C_s symmetry, and passes through the global minimum. mSPCFw, CHON-2017_weak and water-2017 predict water dimer binding energies of 28.60 kJ mol^{-1}, 26.32 kJ mol^{-1} and 27.66 kJ mol^{-1} respectively. These values are around double the experimental value[92] of $D_0^{dim} = (13.2 \pm 0.1)$ kJ mol^{-1} (including NQEs), or if comparing the potential energy surface without NQEs, $\sim$30-50% higher than the $D_e^{dim} \sim 20$ kJ mol^{-1} predicted by
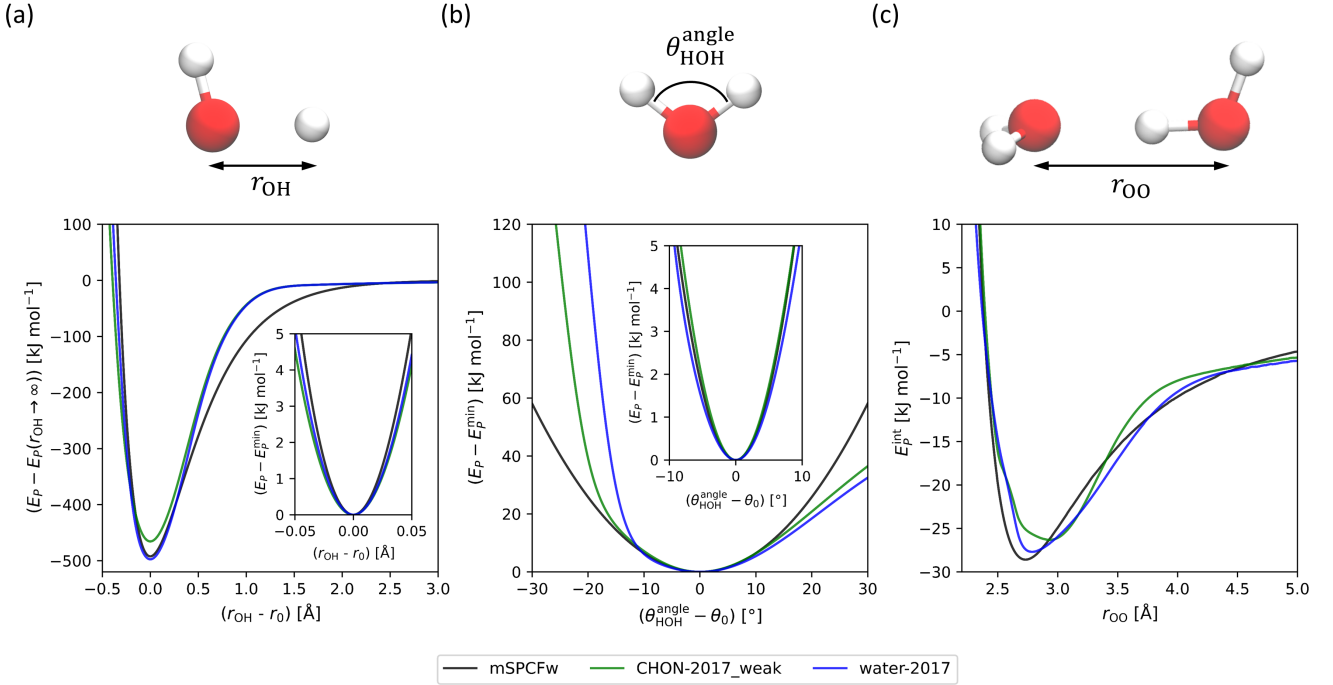
FIG. 6. Potential energy curves (PECs) of the water monomer and dimer as predicted by the CHON-2017_weak and water-2017 ReaxFF water models, as well as the mSPCFw force field. (a) The water monomer bond dissociation PEC: the potential energy E_P as a function of $r_{OH} - r_0$, where r_{OH} is the oxygen-hydrogen distance and r_0 is the distance at the minimum-energy geometry; E_P is shifted relative to its value at infinite separation $E_P(r_{OH} \to \infty)$. The inset shows E_P relative to that of the minimum-energy geometry E_P^{min}, close to r_0. (b) The angle-strain PEC: $E_P - E_P^{min}$ as a function of $\theta_{HOH}^{angle} - \theta_0$, where θ_{HOH}^{angle} is the H-O-H angle, and θ_0 is θ_{HOH}^{angle} at the minimum-energy geometry. (c) The interaction energy $E_P^{int} = E_P^{min}((H_2O)_2) - 2E_P^{min}(H_2O)$ of the C_s water dimer as a function of oxygen-oxygen distance r_{OO}.

high-level *ab initio* calculations[93–95]. The RFF training data included DFT (X3LYP/6-311++G**) water dimer PECs that also give $D_e^{dim} \sim 20$ kJ mol^{-1}.[20,21] The order of dimer hydrogen bonding strength conveyed by the binding energies, mSPCFw > water-2017 > CHON-2017_weak, is consistent with the predicted enthalpies of vaporization of bulk water (see section III I). The dimer PEC for CHON-2017_weak features a broader and shallower minimum, similar to the first intermolecular maximum of the O-O RDF of liquid water, which reflects the strength of the hydrogen bonds. However, the RDFs include *n*-body terms arising from interactions of several molecules with a central one and between themselves (see section III A). Indeed, care must be taken when relating the properties of the (single C_s) water dimer to the structure and thermodynamics of bulk water, as many-body effects and configurations other than the optimal hydrogen bonding arrangement contribute to the sampled potential energy surface of bulk water at finite temperature.

E. Density and Thermal Expansion

The equation of state at 1 bar is shown in Fig. 7. The CHON-2017_weak and water-2017 RFFs give average densities of (0.9921 ± 0.0002) g cm^{-3} and (1.0032 ± 0.0001) g cm^{-3} at 300 K respectively; these are in good agreement with

the experimental value[45] of 0.9966 g cm^{-3} at the same temperature and pressure. Our results are consistent with those previously reported at 298.15 K: 0.99 g cm^{-3} for CHON-2017_weak[23] and 1.01 g cm^{-3} for water-2017[21]. mSPCFw predicts a water density of (1.0067 ± 0.0001) g cm^{-3} at 300 K, this is $\sim 2\%$ higher than the value of 0.991 g cm^{-3} at 298 K and 1 atm reported[5] by Smirnov, and is closer to the (1.012 ± 0.016) g cm^{-3} of the original SPCFw model (which shares the same intermolecular potentials) at 298.15 K and 1 atm.[4] SPC/E predicts a density of 0.994 g cm^{-3} at 298.15 K and 1 atm;[96] the experimental value[45] is 0.9971 g cm^{-3}. Thus, the RFFs are of comparable accuracy to these three-point, non-polarizable force fields. Additionally, the RFFs are only marginally less accurate than the TIP4P/2005 model, which predicts 0.9972 g cm^{-3} (0.9979 g cm^{-3}) at 300 K (298 K) and 1 bar,[2,97] within 0.1% of the experimental values.

We additionally compute the volumetric thermal expansion coefficient $\alpha_P = (1/V)(\partial V/\partial T)_P$ using the fluctuation relation $\langle \delta V \delta H \rangle_{NPT} = k_B T^2 V \alpha_P$, where T is temperature, V is volume, H is enthalpy, and k_B is the Boltzmann constant. $\delta \mathscr{A} = \mathscr{A} - \langle \mathscr{A} \rangle_{ens}$ where $\langle \mathscr{A} \rangle_{ens}$ is the ensemble average of variable $\mathscr{A}$. At 300 K we obtain $\alpha_P/(10^{-4}$ K$^{-1})$ values of 2.0 ± 0.2, 3.3 ± 0.2 and 4.4 ± 0.1 for CHON-2017_weak, water-2017 and mSPCFw respectively; these can be compared to the experimental value of $2.7 \cdot 10^{-4}$ K^{-1} calculated from the numerical derivative of the $\rho(T)$ curve[45] shown in Fig. 7.
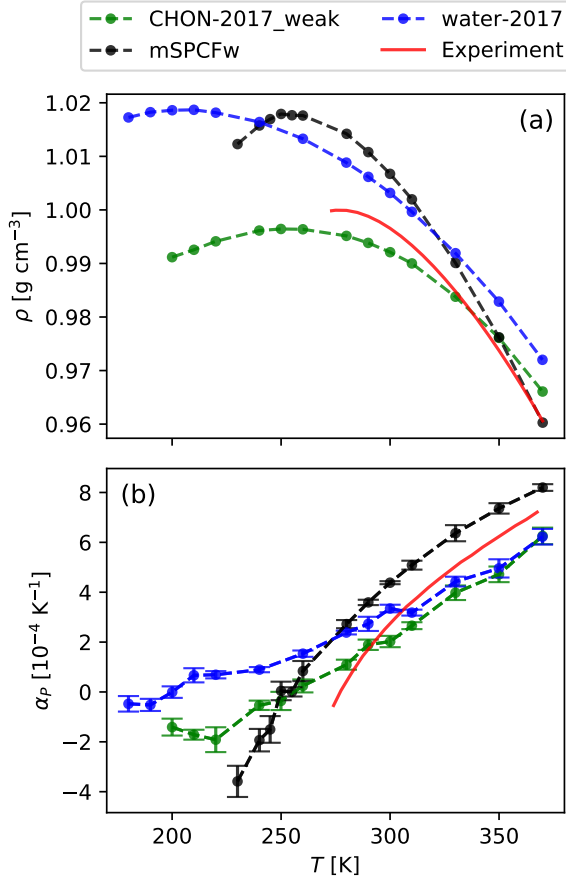
FIG. 7. Density ρ (a) and thermal expansion coefficient α_P (b) of liquid water at temperatures T along the 1 bar isobar, as predicted by the CHON-2017_weak and water-2017 ReaxFF models, as well as the mSPCFw force field. In (a), uncertainties associated with ρ are smaller than the size of the symbols. Experimental values are from Ref. 45.

TIP4P/2005 predicts $\alpha_P = 2.8 \cdot 10^{-4}$ K^{-1} at 298 K and 1 atm, within 10% of the experimental value of $2.56 \cdot 10^{-4}$ K^{-1}.[2]

The competition between hydrogen bond formation and thermal expansion leads to liquid water's anomalous density maximum, which at 1 bar occurs at 277 K.[45] Work by Paschek[98] highlighted the importance of $\rho(T)$ and $\alpha_P(T)$ for describing the hydrophobic effect in water, and in part motivated the emphasis placed on T_{MD} as a target parameter when fitting TIP4P/2005.[2] Both RFFs underestimate the temperature of maximum density T_{MD}, which were estimated by interpolating ρ and α_P: CHON-2017_weak and water-2017 predict (255 ± 3) K and (205 ± 6) K respectively. mSPCFw also underestimates T_{MD} giving (252 ± 3) K, similar to SPC/E with $T_{MD} = 240$-241 K.[1,66] TIP4P/2005 was fit to closely reproduce T_{MD}, even at the expense of a more accurate melting temperature;[2] it therefore unsurprisingly achieves $T_{MD} = (277 \pm 3)$ K in agreement with the experimental value.[1,2,66,97]

F. Enthalpy of Vaporization

The enthalpy of vaporization ΔH_{vap} is the change in enthalpy required to transform n mols of substance from liquid to gas phase, where each phase is under the coexistence pressure (i.e. the vapour pressure of the liquid). $\Delta H_{vap} = H_g(P,T) - H_l(P,T)$ can be written as $\Delta H_{vap} = (U_g - U_l) + P(V_g - V_l)$ where $U = K + E_P$ is the internal energy, K is the kinetic energy and E_P is the potential energy. Noting that $V_g \gg V_l$ and assuming that the gas is ideal ($PV_g = nRT$ and $E_{P,g}^{inter} = 0$), one obtains $\Delta H_{vap} \approx (E_{P,g} - E_{P,l}) + nRT$ where R is the gas constant. Using experimental data, corrections to ΔH_{vap} accounting for the non-ideality of the gas phase have been estimated to be approximately -0.02 kJ mol^{-1} at 298 K, increasing in magnitude with temperature to -0.22 kJ mol^{-1} at 370 K, which is the highest temperature investigated in this work.[99] These corrections have not been taken into account in our ΔH_{vap} values. From our MD simulations we calculate:

$$\Delta H_{vap} \approx \langle E_{P,g}^{intra} \rangle - \langle E_{P,l} \rangle + nRT \quad (6)$$

Simulations of liquid water were carried out at an external pressure of 1 bar, rather than the vapour pressure. This should introduce a minor change in $E_{P,l}$ compared to the potential energy at the state corresponding to the vapour pressure. The difference is expected to be within the uncertainty of the simulation results, $\lesssim 2 \cdot 10^{-3}$ kJ mol^{-1} using Ref. 99 as a guideline. The gas-phase intramolecular potential energies $E_{P,g}^{intra}$ were from simulations of a molecule in vacuum in the NVT ensemble. We do not include a correction for NQEs, as these have been estimated to be small.[99] Nevertheless, the increase of ΔH_{vap} for isotopologues D$_2$O (45.48 kJ mol^{-1}) and T$_2$O (45.73 kJ mol^{-1}) observed experimentally indicate that NQEs are appreciable.[2] NQEs are implicitly included in classical models fit to experimental data (especially since ΔH_{vap} is often used as a target parameter), while this is not the case for RFFs if they are parameterized using only *ab initio* data.

Our results for the enthalpy of vaporization are shown in Fig. 8. All three force fields overestimate ΔH_{vap} compared to the experimental values, water-2017 more severely than CHON-2017_weak for the RFFs. At 300 K CHON-2017_weak, water-2017 and mSPCFw predict ΔH_{vap}/(kJ mol^{-1}) values of 49.27 ± 0.05, 52.09 ± 0.06 and 52.49 ± 0.06, while the experimental value[45,58] is 43.908 ± 0.007. We also compare ΔH_{vap}/(kJ mol^{-1}) at 300 K and 0.997 g cm^{-3}, which is the corresponding experimental density at saturation pressure: 49.30 ± 0.05, 52.05 ± 0.06 and 52.44 ± 0.06 for CHON-2017_weak, water-2017 and mSPCFw respectively. Unsurprisingly, these constant-volume values are similar to their constant-pressure counterparts as all three force fields reproduce the experimental density at 300 K and 1 bar fairly well (see section III E).

Popular rigid non-polarizable models perform much better than the ReaxFF (and mSPCFw) models investigated in this work. Models such as TIP3P, TIP4P and TIP5P reproduce ΔH_{vap} (without a polarization correction) by design and do so to within 5% at 298 K.[1,2] TIP4P/2005 includes the dipole-corrected[3] enthalpy of vaporization $\Delta H'_{vap}$ as a

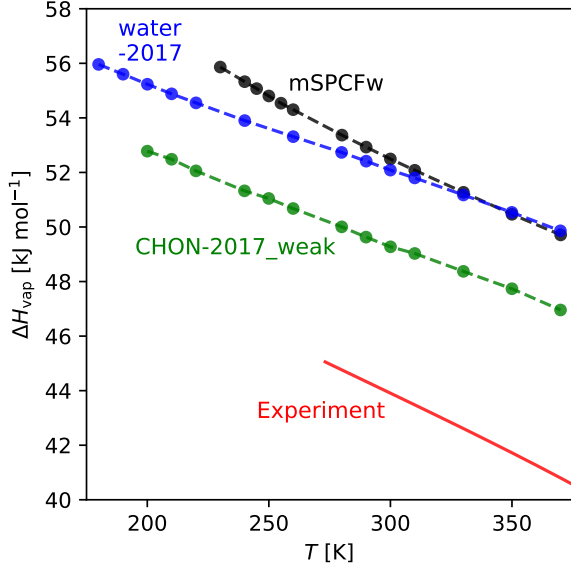FIG. 8. Enthalpy of vaporization ΔH_{vap} at temperatures T predicted by the CHON-2017_weak and water-2017 ReaxFF models, as well as the mSPCFw force field. Uncertainties are smaller than the size of the symbols. Experimental values are from Ref. 45.

target parameter, but its reproduction is a compromise with other target parameters, primarily T_{MD}.[2] Similarly, SPC/E is a reparameterization of SPC accounting for this dipole correction term.[3] Thus at 298 K, TIP4P/2005 and SPC/E predict higher $\Delta H_{vap}/(\text{kJ mol}^{-1})$ values, 50.17 and 49.33, but $\Delta H'_{vap}/(\text{kJ mol}^{-1})$ values, 45.56 and 44.12, in better agreement with experimental value[45,58] of $\Delta H_{vap} = (43.994 \pm 0.007)$ kJ mol^{-1}.[1–3] The dipole correction[3] used in these models amounts to ~ -5 kJ mol^{-1}, and accounts for the intramolecular rearrangement energy required to give the correct gas phase dipole moment. However, recent work has shown that taking into account both multipole distortion and purely electronic polarization effects, up to the quadrupole moment, results in a smaller total correction close to zero.[100] We decided not to include additional corrections since the reference systems in the vapour phase are well defined for each force field. By construction, all three force fields incorporate changes in molecular multipole moments between the liquid and vapour phases: mSPCFw through changes in molecular geometry, and the ReaxFF models through changes in geometry and atomic partial charges.

G. Surface Tension

The surface tension γ is defined as the work required to create one unit area of the interface. In the NVT ensemble, this is given by $\gamma = (\partial F/\partial A)_{NVT}$ where F is the Helmholtz free energy and A is the surface area. We calculate γ based on the mechanical definition for a planar interface perpendicular

to the z-axis:

$$\gamma = \int_{-\infty}^{\infty} [P_N(z) - P_T(z)]dz \qquad (7)$$

where $P_N(z)$ and $P_T(z)$ are the normal and tangential (local) components of the pressure tensor respectively. For a planar interface, P_N is equal to the vapour pressure and is independent of position z. From our MD simulations (see section II A 2), which stabalize two liquid-vapour interfaces, γ can be calculated as

$$\gamma = \frac{L_z}{2}\left(\langle P_{zz}\rangle + \frac{\langle P_{xx}\rangle + \langle P_{yy}\rangle}{2}\right) \qquad (8)$$

where $P_{\alpha\alpha}$, with $\alpha = x, y, z$, are the diagonal components of the pressure tensor.

Density profiles of the interfacial systems and the convergence of γ are shown in Fig. 9. At 300 K, CHON-2017_weak, water-2017 and mSPCFw predict $\gamma/(\text{mN m}^{-1})$ values (percent errors) of 67 ± 2 (-4-9%), 59 ± 1 (-17-20%) and 63 ± 1 (-9-14%) compared to the experimental value[59] of 71.7 ± 0.4. TIP4P/2005 predicts $\gamma = 68\text{-}69$ mN m^{-1} (-4-5%) at 300 K, with simulation uncertainties of ±1 mN m^{-1} typically being reported.[1,101–103] Thus, while water-2017 substantially underestimates the surface tension, CHON-2017_weak predicts γ in relatively good agreement with experiment: only $\sim3\%$ lower than TIP4P/2005, and more accurately than many other[1,102–105] classical force fields.

Since the liquid-vapour interface simulations were carried out using a single box with dimensions $(30, 30, 200)$ Å, it is not possible to perform a finite-size analysis for the surface tension values. However, the lateral dimensions $L_x = L_y = 30$ Å $\approx 9.5\sigma$ were chosen to ensure finite-size effects are small if not insignificant; for TIP4P/2005, γ values calculated with lateral dimensions of 7σ, 9.5σ and 11.3σ were found to agree with each other to within their associated uncertainties of ≤ 1.3 mN m^{-1}. Regarding the finite slab thickness, all three systems possess Gibbs dividing surfaces separated by 33-34 Å of liquid, as determined fitting hyperbolic tangent functions to the density profiles. Negative vapour pressures $P_{vap} = P_{zz}$ were obtained for all three force fields: (-0.64 ± 0.02) bar, (-0.67 ± 0.05) bar and (-0.71 ± 0.02) bar for CHON-2017_weak, water-2017 and mSPCFw respectively. This has previously[101,102] been observed for temperatures as low as 300 K, and is presumably due to the disjoining pressure that arises from the attractive forces between the two surfaces. The measured surface tensions are therefore systematically underestimated by 0.6-0.8 mN m^{-1} (assuming $P_{vap} \sim 10^{-2}$ bar), which is within their associated statistical uncertainties.

H. Isothermal Compressibility

Water is generally approximated as an in-compressible fluid at ambient temperature and pressure conditions. The isothermal compressiblity $\beta_T = -(1/V)(\partial V/\partial P)_T$ was calculated from our MD simulations using the fluctuation relation $\langle \delta V^2\rangle_{NPT} = Vk_BT\beta_T$. Our results for β_T are shown in
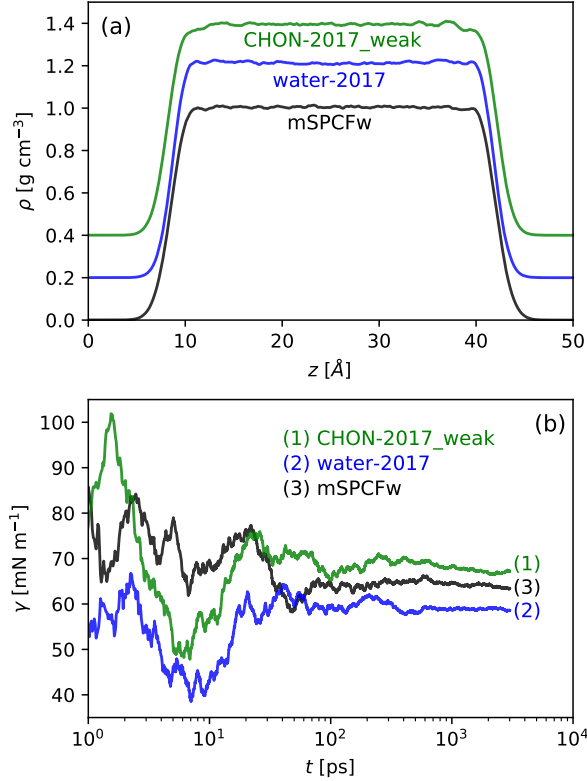
FIG. 9. (a) Density ρ profiles of the liquid-vapour interface systems along the z-axis perpendicular to the interface. For clarity, the density profiles of water-2017 and CHON-2017_weak have been shifted vertically by 0.2 g cm^{-3} and 0.4 g cm^{-3} respectively. (b) Convergence of the the surface tension γ with simulation time t.

FIG. 10. Isothermal compressibility β_T of liquid water at temperatures T along the 1 bar isobar, as predicted by the CHON-2017_weak and water-2017 Reaxff models, as well as the mSPCFw force field. Experimental values are calculated from Ref. 45.

Fig. 10 and Table II. The RFFs both underestimate β_T for the temperature range investigated. At 300 K, this underestimation is by $\sim$15% for CHON-2017_weak (β_T/Mbar^{-1} = 38.2 $\pm$ 0.3) and $\sim$29% for water-2017 (β_T/Mbar^{-1} = 31.8 $\pm$ 0.1), compared to the experimental value[45] of 45.1 Mbar^{-1}. For mSPCFw, β_T values coincide with experiment at $\sim$315 K, with departing agreement at both higher and lower temperatures. At 300 K, mSPCFw predicts $\beta_T = (42.5\pm0.2)$ Mbar^{-1}, in good agreement with experiment. Indeed, popular classical models seem to offer more accurate β_T predictions compared to the RFFs, with TIP4P/2005 and SPC/E giving 46.5 Mbar^{-1} and 46.1 Mbar^{-1} respectively at 298 K and 1 bar,[2,97] which can be compared to the experimental value[45] of 45.3 Mbar^{-1}.

The decrease in isothermal compressibility with increasing temperature until a minimum at $T_{\beta_{T,\min}}$, and the minimum itself, are considered two of the anomalous properties of water. At 1 bar, this β_T minimum occurs at 319 K.[45] Some classical models of water are able to reproduce this minimum, such as TIP4P/2005 and SPC/E, while others such as TIP5P are not.[66,97] TIP4P/2005 predicts $T_{\beta_{T,\min}}$ around 310-320 K,[66,97] while SPC/E predicts a value of $\sim$280 K.[66] Fitting a cubic function to the $\beta_T(T)$ data for CHON-2017_weak suggests that a minimum exists at $T_{\beta_{T,\min}} = (260\pm40)$ K, in close prox-
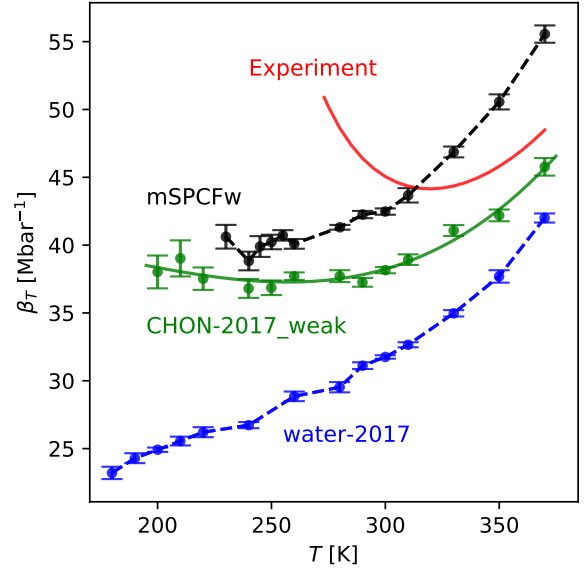
imity to its temperature of maximum density. However, owing to the statistical uncertainty associated with β_T values for $T \leq 250$ K, we do not discount the possibility that the minimum disappears upon more exhaustive sampling. As shown in Fig. 10, water-2017 features a monotonic increase in β_T with temperature, and thus does not capture the minimum, nor the decreasing β_T for $T < T_{\beta_{T,\min}}$. Likewise, a minimum is not observed for mSPCFw; as temperature is decreased along the isobar, β_T decreases then plateaus near T_{MD}.

High energy x-ray diffraction experiments show a continuous structural transition associated with the second g_{OO} peak position concomitant with the compressibility minimum, with greater tetrahedral order being observed at and below $T_{\beta_{T,\min}}$.[63] The increase from near-zero intensity at $g_{OO}(r_{OO}/\text{Å} \simeq 11)$ peak from 340-320 K upon cooling further suggests that tetrahedral structures start to appear as well-defined regions around the compressibility minimum.[106] Longer range correlations also indicate a restructuring of the liquid, favouring tetrahedral H-bonding, upon cooling.[107] Two-state models[108–111] (which have garnered increasing support from experimental data) rationalize the anomalous properties of water, including the compressibility minimum, in terms of structural fluctuations between low-density liquid (enthalpy favoured through tetrahedral H-bonding) and high-density liquid (entropy favoured with a more close-packed structure, possessing a fifth neighbour in the interstitial position between the first and second coordination shells).[112] Water models that do not possess a compressibility minimum fail to capture these structural properties of water. The lack of a compressibility minimum for water-2017 indicates that this RFF is missing crucial aspects of the orientational correlations

in liquid water, since these are linked to the tetrahedral order of the liquid.

I. Isobaric and Isochoric Heat Capacity

An unusually high heat capacity is considered one of the anomalous properties of water, and is rationalised in terms of water's strong hydrogen bonding. Under thermodynamic constraints of constant pressure and constant volume, the isobaric $C_P = (\partial H/\partial T)_P$ and isochoric $C_V = (\partial U/\partial T)_V$ heat capacities can be written in terms of thermodynamic potentials H and U. We compute these heat capacities from MD simulations using the fluctuation relations $\langle \delta H^2 \rangle_{NPT} = k_B T^2 C_P$ and $\langle \delta U^2 \rangle_{NVT} = k_B T^2 C_V$. C_V values corresponding to 300 K and 0.997 g cm^{-3} were calculated from NVT simulations (see Table I), while C_P values at 1 bar were calculated from NPT simulations. Additionally, C_V values along the 1 bar isobar were calculated using the relation

$$C_P = C_V + VT\frac{\alpha_P^2}{\beta_T} \qquad (9)$$

where all variables in Eq. III I can be measured from our NPT simulations. We obtain consistent values of C_V at 300 K (corresponding to slightly different average densities) via Eq. III I and the $\langle \delta U^2 \rangle_{NVT}$ fluctuation relation.

As evident in Fig. 11 values of C_P and C_V are overestimated by $\sim$30-60%, primarily due to the exclusion of NQEs. At 298 K, D$_2$O (C_V=84.42 kJ mol^{-1})[113] has a heat capacity 13% greater than H$_2$O (C_V=74.55 kJ mol^{-1})[45], indicating that the overall impact of NQEs is to reduce the heat capacity. Path-integral simulations incorporate NQEs by treating nuclei quantum mechanically, and when paired with a suitable potential energy surface, are able to accurately reproduce the heat capacities of H$_2$O and D$_2$O.[114] Extracting "quantum" heat capacities from classical simulations requires further approximations. The most widely adopted approach is to quantum-correct the vibrational density of states $S(\nu)$, as in the 1PT model[115], the 2PT model[116–118] and the correction of Berens[115]. Similar corrections can be applied directly to the VACF and trajectories.[119] These methods have previously been applied to liquid water.[115,119–122] The main advantage of the 2PT model is that only $S(\nu)$ and therefore short MD trajectories are required, while the correction of Berens has been shown to better account for NQEs in liquid water.[119] Additionally, the original 2PT method is not equipped to deal with bond breaking and formation.[123]

In this work we employ the method[115] of Berens, and quantum-correct C_V within a harmonic oscillator approximation.[115]

$$C_V^{qc} = C_V + C_V^\Delta \qquad (10)$$

This involves integrating $S(\nu)$ with a weighting function $W_{C_V}^\Delta$, which is the difference between the quantum and classical weighting functions for a set of harmonic oscillators:

$$C_V^\Delta = k_B \int_0^\infty S(\nu) W_{C_V}^\Delta \, d\nu \qquad (11)$$

$$W_{C_V}^\Delta = \frac{u^2 e^u}{(1-e^u)^2} - 1 \qquad (12)$$

where $u = h\nu/(k_B T)$ and h is Planck's constant. $S(\nu)$ was obtained from the Fourier transform of the total VACF $C(t)$, defined as the mass-weighted sum of atomic VACFs,

$$C(t) = \sum_{j=1}^{N} m_j \langle \mathbf{v}_j(t_0+t) \cdot \mathbf{v}_j(t_0) \rangle \qquad (13)$$

$$S(\nu) = \frac{2}{k_B T} \lim_{\tau \to \infty} \int_{-\tau}^{\tau} C(t) e^{-i2\pi\nu t} dt \qquad (14)$$

where m_j and $\mathbf{v}_j$ are the mass and velocity of atom j respectively, and t is the elapsed time from arbitrary starting time t_0. $S(\nu)$ has the normalization $\int_0^\infty S(\nu)d\nu = 3N$ where N is the total number of degrees of freedom (9 per molecule for flexible water models).

This approach satisfies the correspondence principle $\lim_{\hbar \to 0} C_V^{qc} = C_V$. While C_V^Δ does not incorporate anharmonic effects, they are included through the classical C_V. The quantum correction C_V^Δ is based on the division of dynamics in frequency space. The low-frequency region features major anharmonic effects but behaves nearly classically, so while the correction is less accurate, it is small. At higher frequencies, atomic motions are better approximated as harmonic and quantum effects are more significant, so while the correction is large, it is also reasonably accurate. Thus, the quantum correction can be applied over the entire frequency domain.

C_V^Δ values were calculated from MD simulations in the NVT ensemble with production runs spanning 500 ps. For simulations corresponding to the 1 bar isobar, the average densities from the NPT simulations were used. We show in Table V that the thermostat and reducing the timestep do not have an appreciable effect on C_V^{qc} (see Table V for numerical values).

At 1 bar the quantum-corrected heat capacities C_P^{qc} (C_V^{qc}) of the RFFs are systematically underestimated: for example, by $\sim$7% ($\sim$7%) for CHON-2017_weak and $\sim$16% ($\sim$17%) for water-2017 at 300 K. Similarly C_V^{qc} at 300 K and 0.997 g cm^{-3} is underestimated by $\sim$9% and $\sim$18% for CHON-2017_weak and water-2017 respectively. Once quantum-corrected, mSPCFw predicts heat capacities that are in relatively good agreement with experiment in the temperature range corresponding to liquid water. C_P^{qc} deviates from experiment by just $\sim$3% at 300 K and 1 bar, and the C_V^{qc} values corresponding to 300 K (both at 1 bar and 0.997 g cm^{-3}) agree with experiment withing their associated uncertainties. The C_P^{qc} values agree with experiment considering their associated uncertainties for $310 \leq T/K \leq 370$. With $C_P = 88.3$ J K^{-1} mol^{-1} at 298 K and 1 bar, TIP4P/2005 overestimates C_P by $\sim$7%;[2] quantum-corrections bring C_V^{qc} to within $\sim$3% of the experimental value.[121] Rigid models are expected to have smaller heat capacities and quantum corrections than their flexible counterparts, as intramolecular modes are frozen
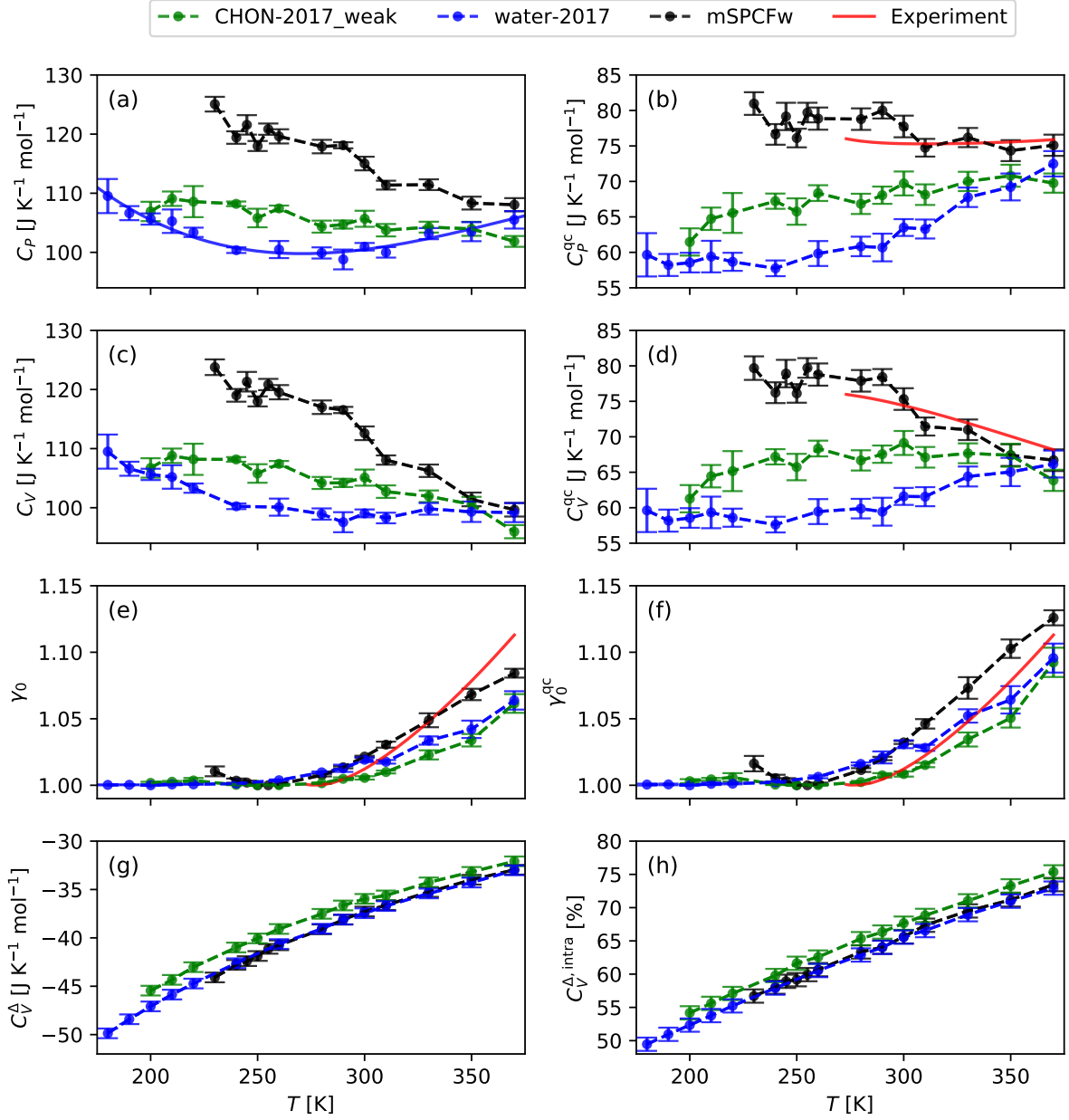
FIG. 11. Heat capacities and related quantities of liquid water at temperature T along the 1 bar isobar, as predicted by the CHON-2017_weak and water-2017 Reaxff models, as well as the mSPCFw force field: (a) isobaric heat capacity C_P, the solid line is a cubic function fit to the water-2017 data; (b) quantum-corrected isobaric heat capacity C_P^{qc}; (c) isochoric heat capacity C_V; (d) quantum-corrected isochoric heat capacity C_V^{qc}; (e) heat capacity ratio $\gamma_0 = C_P/C_V$; (f) quantum-corrected ratio $\gamma_0^{\mathrm{qc}} = C_P^{\mathrm{qc}}/C_V^{\mathrm{qc}}$; (g) quantum correction C_V^{Δ}; and (h) intramolecular contribution $C_V^{\Delta,\mathrm{intra}}$ to the quantum-correction. Experimental values are from or calculated from Ref. 45.

out. Path-integral simulations with TIP4PQ/2005 underestimate C_P by ∼6% at 300 K.[114]

At 1 bar, the isobaric heat capacity of water has a minimum at ∼310 K.[45] Interestingly, water-2017 features a shallow minimum in C_P at (270 ± 30) K as determined by fitting a cubic function. This minimum is either lost or moved to a lower temperature, upon applying the quantum correction. mSPCFw and CHON-2017_weak do not possess a discernible

minimum in either C_P or C_P^{qc} in the temperature interval considered here.

$|C_V^{\Delta}|$ increases with decreasing temperature primarily through $W_{C_V}^{\Delta}$ (Eq. III I); the temperature dependence of $S(\nu)$ also serves to decrease $|C_V^{\Delta}|$, but to a much lesser extent. The quantum corrections C_V^{Δ} differ by at most ∼2 J K^{-1} mol^{-1} between the RFFs and mSPCFw, while corrections for rigid models are substantially smaller.[121] We partition C_V^{Δ}

into intramolecular and intermolecular contributions by dividing $S(\nu)$ at frequency ν_{cut} corresponding to the minimum between the libration peak and bending peak of a smoothed $S(\nu)$. The value of ν_{cut} therefore depends on the force field and thermodynamic conditions, and falls in the range 1200-1600 cm^{-1} for the thermodynamic states considered in this work. This partitioning method incurs some systematic error since intermolecular (intramolecular) interactions contribute to $S(\nu > \nu_{cut})$ ($S(\nu < \nu_{cut})$). However, this systematic error is likely small since $S(\nu_{cut}) \approx 0$, and owing to the expected cancellation of errors. The intramolecular contribution $C_V^{\Delta,\text{intra}}$ constitutes ~66-68% of C_V^Δ at 300 K, and increases with temperature, again primarily due to the $k_B T$ terms in $W_{C_V}^\Delta$.

We additionally show the ratios $\gamma_0 = C_P/C_V = 1 + VT\alpha_P^2/\beta_T$ and $\gamma_0^{qc} = C_P^{qc}/C_V^{qc}$, which show qualitatively the same temperature dependence as experiment. $\gamma_0^{qc} > \gamma_0$ as expected from $C_V^\Delta < 0$.

J. Speed of Sound

In classical mechanics, the speed of sound c is given by $c^2 = dP/d\rho$. The isentropic (adiabatic) speed of sound can therefore be written in terms of the isentropic compressibility β_S as

$$c_S^2 = \frac{1}{\rho\beta_S}, \tag{15}$$

which we calculate in turn from our *NPT* simulations at 1 bar using the relation

$$\beta_S = \beta_T - \frac{\alpha_P^2 T}{\rho C_P}. \tag{16}$$

We further calculate c_s^{qc} using the quantum-corrected isobaric heat capacity C_P^{qc} in Eq.III J. The results are shown in Fig. 12. The inability of all three force fields to reproduce the experimental trend in c_S can be attributed primarily to their β_T values, with ρ being fairly well reproduced (see section III E), and the $\alpha_P^2 T/(\rho C_P)$ term contributing between 0-8% of β_T (0-12% using C_P^{qc}) across the temperature range (e.g. 1-2% at 300 K). This is also evidenced by the $\gamma = C_P/C_V = \beta_T/\beta_S \approx 1$ values shown in Fig. 11, and the relatively minor impact quantum-correcting C_P has on c_S. Nevertheless, mSPCFw predicts $c_S = (1551 \pm 4)$ m s^{-1} at 300 K, just 3-4% from the experimental value of 1501.5 m s^{-1}. mSPCFw and CHON-2017_weak predictions coincide with experiment at ~316 K (in line with β_T, see section III H) and ~370 K respectively. At 300 K, CHON-2017_weak and water-2017 predict c_S/(m s^{-1}) values (percent errors) of 1629±7 (8-9%) and 1789±4 (19%) respectively.

At 1 bar, c_S has a maximum at 347 K, in close proximity to the compressibility minimum. Fitting a cubic functions to the $c_S(T)$ and $c_S^{qc}(T)$ data for CHON-2017_weak suggests that a maximum exists at $T_{c_{S,\max}} = (260 \pm 40)$ K for both sets of data, coincident with the compressibility minimum. water-2017 predicts monotonically decreasing c_S values with increasing temperature, and a maximum at $T > T_{MD}$ is also not
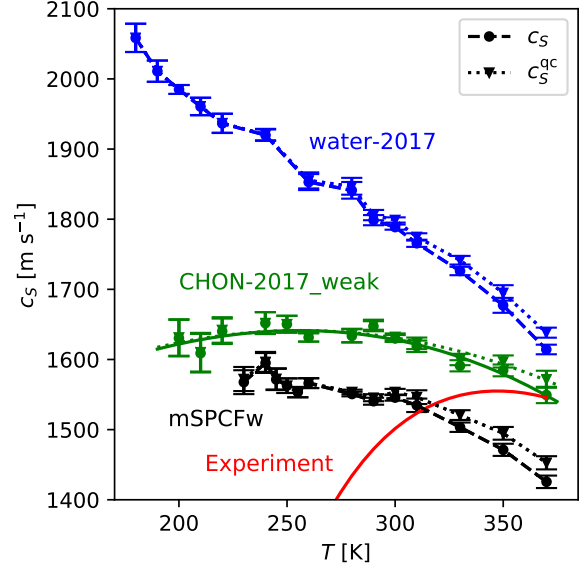

FIG. 12. Isentropic speed of sound of liquid water at temperatures T along the 1 bar isobar, as predicted by the CHON-2017_weak and water-2017 Reaxff models, as well as the mSPCFw force field. c_S and c_S^{qc} are the classical and quantum-corrected speed of sound respectively. For CHON-2017_weak, the solid and dotted lines show cubic functions fit to the c_S and c_S^{qc} data respectively. Experimental values are from Ref. 45

observed for mSPCFw, similar to the β_T minimum. Classical force fields that are better able reproduce β_T along the 1 bar isobar, will presumably also more accurately predict c_S. For example, TIP4P/2005 predicts c_S in excellent agreement with experiment at 1 bar and temperatures close to 300 K.[124,125]

K. Self-Diffusion Coefficient

We calculate the self-diffusion coefficients D from the average mean square displacement (MSD) using the Einstein relation

$$D = \frac{1}{2d}\lim_{t\to\infty}\frac{\langle|\boldsymbol{r}(t+t_0) - \boldsymbol{r}(t_0)|^2\rangle}{t} \tag{17}$$

where t is the elapsed time from arbitrary starting time t_0, and $d = 3$ is the number of spatial dimensions. D was therefore calculated by fitting to the equation $\langle|\boldsymbol{r}(t) - \boldsymbol{r}(0)|^2\rangle = 6Dt$, excluding the first 10 ps of data to ensure only the diffusive regime was sampled (as opposed to the ballistic regime). In order to account for finite-size effects, we calculate the "infinite-size" diffusion coefficient D_0 by extrapolation to $L^{-1} = 0$, where L is the length of the cubic simulation box. This finite-size analysis is shown in Fig. 13, and follows from the equation derived by Yeh and Hummer[126] using a simple hydrodynamic model of a particle surrounded by a solvent of viscosity η_{YH} in a periodically replicated simulation box,

$$D_{PBC} = -\frac{\xi k_B T}{6\pi\eta_{YH}}L^{-1} + D_0 \tag{18}$$

where D_{PBC} are the finite-size diffusion coefficients calculated from our MD simulations, and ξ is a dimensionless constant equal to 2.837297 for a cubic simulation box with 3D periodic boundary conditions.[126] The same expression was obtained earlier[127] by Dünweg and Kremer using a closely related derivation. Equation 18 also provides a route to estimate the shear viscosity η. From the fitted gradients and intercepts in Fig. 13, it is evident that force fields that predict higher diffusion coefficients also predict lower viscosities, consistent with $D \propto \eta^{-1}$ implied by the Stokes-Einstein relation.

Values for the diffusion coefficients D_0 are shown in Table. I. We compare our results to a reference value[55] of $(2.41 \pm 0.02) \cdot 10^{-5}$ cm^2 s^{-1} at 300 K, as determined from a Speedy-Angell power-law fit to experimental data. Both RFFs overestimate the self-diffusion coefficient: by 22% for CHON-2017_weak and 51% for water-2017. This is particularly unfortunate for the water-2017 force field, which was designed in part to predict more accurate OH$^-$/H$_3$O$^+$/H$_2$O diffusion compared to its predecessor.[20,21] Fitting to Eq. 18, our value of $D_{\text{PBC}} = (3.0 \pm 0.1) \cdot 10^{-5}$ cm^2 s^{-1} for $N = 216$ water molecules ($L \approx 18.64$ Å) is consistent with the value of $2.7 \cdot 10^{-5}$ cm^2 s^{-1} reported by Ref. 21 – a slightly lower diffusion coefficient is expected at 298.15 K and 1.01 g cm^{-3}. For CHON-2017_weak, a diffusion coefficient of $2.5 \cdot 10^{-5}$ cm^2 s^{-1} has previously been calculated[23] at 298.15 K and 0.99 g cm^{-3}, but system sizes were not reported alongside this value, so a fair comparison to our results cannot be made. These literature values[21,23] can be compared to the experimental value[55,128] of $(2.299 \pm 0.005) \cdot 10^{-5}$ cm^2 s^{-1} at 298.15 K, but these simulation results do not account for finite-size effects. However, as demonstrated in this and other[126,129] work, finite-size effects can lead to strong underestimations for small system sizes. The latter are commonly used in *ab initio* MD simulations of liquid water,[14] and care should therefore be exercised when comparing these results with experimental data. For the PBE functional (not accounting for NQEs), D_0 was estimated[130] to be $0.789 \cdot 10^{-5}$ cm^2 s^{-1} at 300 K, which is greatly underestimated compared to experiment.

The size-independent D_0 values vary appreciably between traditional classical force fields, but popular models typically outperform the RFFs, or perform similarly to CHON-2017_weak. In this work, we find mSPCFw predicts $D_0 = (2.40 \pm 0.03) \cdot 10^{-5}$ cm^2 s^{-1} in good agreement with the experimental value. At 300 K and 0.998 g cm^{-3}, TIP4P/2005, SPC/E and the polarizable Dang-Chang model predict $(2.49 \pm 0.05) \cdot 10^{-5}$ cm^2 s^{-1}, $(2.97 \pm 0.05) \cdot 10^{-5}$ cm^2 s^{-1} and $(2.72 \pm 0.09) \cdot 10^{-5}$ cm^2 s^{-1} respectively, slightly higher than experiment.[129] TIP3P predicts $(6.10 \pm 0.03) \cdot 10^{-5}$ cm^2 s^{-1} at 298 K and the lower density of 0.987 g cm^{-3}.[126]

In order to target a specific thermodynamic state, the NVT ensemble was sampled using a temperature control algorithm that alters dynamics compared to the Newtonian dynamics of the NVE ensemble. It is therefore necessary to check whether the employed global Nosé-Hoover (3-chains) thermostat affects the computed self-diffusion coefficients. We demonstrate in Table V, using mSPCFw, that it does not: all D_{MD} values calculated at the same temperature (304 K) agree within their associated uncertainty. This is consistent with
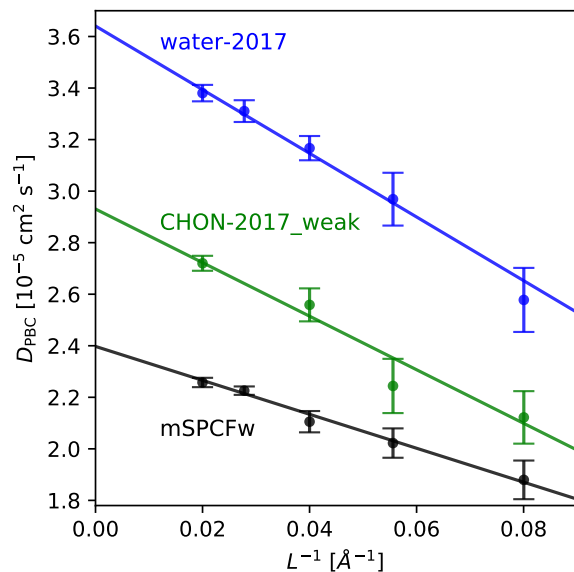

FIG. 13. Finite-size analysis for the self-diffusion coefficients of liquid water at 300 K and 0.997 g cm^{-3}, as predicted by the CHON-2017_weak and water-2017 Reaxff models, as well as the mSPCFw force field. Extrapolation of size-dependent diffusion coefficients D_{PBC} to $L^{-1} = 0$, where L is the length of the cubic simulation box.

previous work that shows that "global" velocity scaling thermostats, including the Nosé-Hoover thermostat, do not significantly alter diffusion coefficients or viscosity.[131] We additionally show in Table V that reducing the timestep to 0.1 fs does not affect the dynamical properties, D and η.

The scope of this work is limited to pure water. However, both the water-2017 and CHON-2017_weak force fields have been used to study the transport of H$^+$ and OH$^-$ ions.[21,25,27,28,30,31] At room temperature and pressures close to 1 bar, the diffusion coefficient of H$_3$O$^+_{\text{(aq)}}$ (OH$^-_{\text{(aq)}}$) were estimated to be $10.4 \cdot 10^{-5}$ cm^2 s^{-1} ($7.8 \cdot 10^{-5}$ cm^2 s^{-1}) and $10.9 \cdot 10^{-5}$ cm^2 s^{-1} for water-2017[21] (at 298.15 K) and CHON-2017_weak[25] respectively. Based on the number of molecules and average densities reported in refs. 21,25, we estimate that the diffusion coefficients correspond to box lengths of $L \approx 18.6$ Å and $L \approx 24.7$ Å for water-2017 and CHON-2017_weak, respectively. These diffusion coefficients appear to be in good agreement with the experimentally determined diffusion coefficients[132] of $9.3 \cdot 10^{-5}$ cm^2 s^{-1} for H$_3$O$^+_{\text{(aq)}}$ and $5.6 \cdot 10^{-5}$ cm^2 s^{-1} for OH$^-_{\text{(aq)}}$, corresponding to 298.15 K and infinite dilution. However, the simulated values do not account for finite-size effects and correspond to finite concentrations, but with no direct solute-solute interactions. Based on the finite-size analysis presented in Fig. 13, the absolute difference in the self-diffusion coefficient of water when going from $L \approx 18.6$ Å for water-2017 and $L \approx 24.7$ Å for CHON-2017_weak, to $L \to \infty$, amount to ~18% and ~14% (relative to D_0), respectively. While we do not necessarily expect the same system size dependence for H$_3$O$^+_{\text{(aq)}}$ and OH$^-_{\text{(aq)}}$, the changes in bulk water are large enough to warrant further in-

TABLE V. The effect of thermostat and timestep δt on the dynamics of mSPCFw water. Results correspond to a 521-molecule water-box with a density of 0.997 g cm^{-3} and average simulation temperature T. $D_{N=521}$, η_{GK} and C_V^Δ are the self-diffusion coefficient, Green-Kubo shear viscosity (Eq. 19) and quantum-correction to the isochoric heat capacity (Eq. III I) respectively. Statistical uncertainties in the least significant figure are given in parentheses.

Ensemble	δt [fs]	T [K]	$D_{N=521}$ [10^{-5} cm^2 s^{-1}]	η_{GK} [mPa s]	C_V^Δ [J K^{-1} mol^{-1}] [a]
NVE	0.1	304	2.28(5)	0.76(6)	−37.3(3)
NVE	0.2	304	2.31(3)	0.73(4)	−37.3(4)
NVT[b]	0.2	304	2.30(7)	0.79(6)	−37.2(4)
NVT[b]	0.2	300	2.11(4)	0.85(1)	−37.3(5)

[a] C_V^Δ is a thermodynamic property. However, it is calculated from the vibrational density of states, and is consequently determined by the dynamics of the system.
[b] Nosé-Hoover chain thermostat with 3 chains (see section II).

vestigation; an extrapolation to infinite system size and infinite dilution would be required to assess the importance of finite-size effects for the diffusion coefficients of these ions.

L. Shear Viscosity

We calculate the shear viscosity η using two methods: the Green-Kubo relation and Eq. 18 (see section III K). The former calculates η using the integral formula

$$\eta_{\mathrm{GK}} = \frac{V}{k_{\mathrm{B}}T} \int_0^\infty C_{P_{\alpha\beta}}(t)dt \tag{19}$$

$$C_{P_{\alpha\beta}}(t) = \langle P_{\alpha\beta}(t_0)P_{\alpha\beta}(t_0+t)\rangle \tag{20}$$

where V is the volume of the simulation box, t is the elapsed time from arbitrary start time t_0, and $C_{P_{\alpha\beta}}(t)$ is the auto-correlation function of off-diagonal components of the pressure tensor $P_{\alpha\beta}$, where $\alpha \neq \beta$. Results were averaged over $(\alpha,\beta) = (x,y)$, (x,z) and (y,z). A correlation time of $t_c = 10$ ps was used for the upper limit in the integral given above. Selecting this integration limit is a compromise between sampling efficiency and minimising the resulting truncation error. We show in Fig. 14 that 10 ps is sufficiently long to achieve a well-converged integral, while the exhaustive extent of our sampling is reflected in the associated statistical uncertainty.

Our calculated values for shear viscosity are shown in Table. I. For all three force fields, the viscosities evaluated using Eq. 18 and Eq. 19, η_{YH} and η_{GK} respectively, agree with each other given their associated uncertainties. Both RFFs underestimate the viscosity compared to the experimental value[56] of (0.854 ± 0.009) mPa s at 300 K and 1 bar: by $\sim$19-26% for CHON-2017_weak and $\sim$34-39% for water-2017, while the mSPCFw values agree with experiment considering their associated uncertainties. Traditional classical force fields typically underestimate η near standard conditions, for example at 298 K and 1 bar with $\eta/$(mPa s) values (percent errors) of 0.321 (-64%) for TIP3P, 0.494 (-45%) for TIP4P, 0.699 (-22%) for TIP5P, 0.855 (-4%) for TIP4P/2005, and 0.729 (-18%) for SPC/E[133], compared to the experimental value[55] of 0.893 ± 0.009. Closer to the thermodynamic conditions used in this work, at 300 K and 0.9965 g cm^{-3}, TIP4P/2005 and SPC/E predict (0.83 ± 0.01) mPa s (-3%) and $(0.722 \pm$
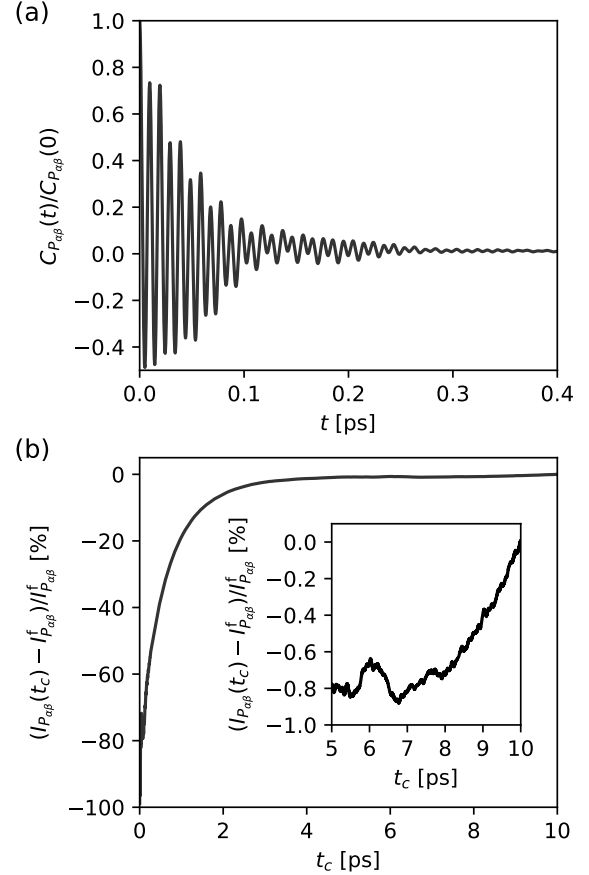
FIG. 14. Convergence tests for the calculation of viscosity using the Green-Kubo integral formula. (a) The normalised autocorrelation function $C_{P_{\alpha\beta}}(t)/C_{P_{\alpha\beta}}(0)$, where t is the elapsed time. (b) The convergence of the integral $I_{P_{\alpha\beta}}(t_c) = \int_0^{t_c} C_{P_{\alpha\beta}}(t)dt$ where t_c is the correlation time used as the upper limit of the integral; $(I_{P_{\alpha\beta}}(t_c) - I_{P_{\alpha\beta}}^{\mathrm{f}})/I_{P_{\alpha\beta}}^{\mathrm{f}}$ is the relative deviation of $I_{P_{\alpha\beta}}(t_c)$ from the final value $I_{P_{\alpha\beta}}^{\mathrm{f}} = I_{P_{\alpha\beta}}(t_c/\mathrm{ps} = 10)$ used to calculate the viscosity.

$0.005)$ mPa s (-15%) respectively.[134] The underestimation by the RFFs is comparable to this range.

We demonstrate in Table V, using mSPCFw, that the employed thermostatting procedure does not significantly alter

η_{GK} values. Additionally, since the thermostat does not significantly affect the self-diffusion coefficients (see section III K), it is not expected to affect η_{YH}.

M. Thermal Conductivity

We calculate the thermal conductivity λ from boundary-driven NEMD simulations using Fourier's Law:

$$\boldsymbol{J}_q = -\lambda \nabla T \qquad (21)$$

where $\boldsymbol{J}_q$ is the heat flux and ∇T is the local temperature gradient. The computation of thermal conductivity via NEMD includes all possible coupling effects; in the case polar fluids such as water this includes the coupling between heat and polarization fluxes.[135,136]

The simulation details and results are summarised in Table VI, and representative temperature profiles are shown in Fig. 15. Local densities ρ and temperatures T were determined from a 5 Å bin close to the centre of each NVE compartment. The position of the bin was chosen such that $T = 300$ K. The local temperature gradient was determined by fitting a straight line to the temperature profile within a range of ± 8 Å around the selected state point; exceptions to this are noted in Table VI.
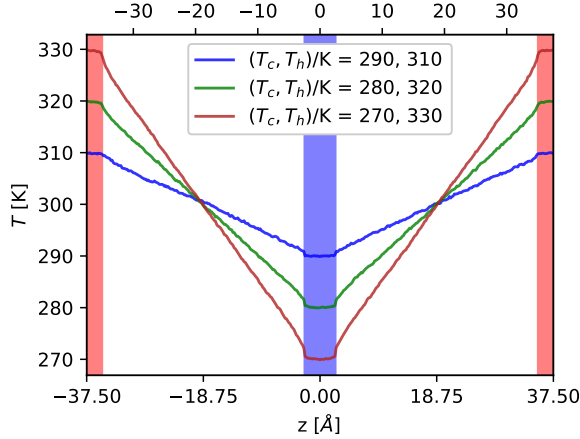

FIG. 15. Representative temperature T profiles for the NEMD simulations. The coordinate z is in the direction parallel to the heat flux. Data corresponds to the CHON-2017_weak ReaxFF model and $L_z = 75$ Å. The blue (cold) and red (hot) shaded areas indicate the location of the thermostatting regions in the simulation box, which were set to temperatures T_c and T_h respectively.

All the NEMD thermal conductivity values calculated in this work, for both ReaxFF and mSPCFw, range from 0.80-0.88 W K^{-1} m^{-1}, and are therefore overestimated by 31-44% relative to the experimental value[57] of (0.609 ± 0.004) W K^{-1} m^{-1} at 300 K and 1 bar. CHON-2017_weak, water-2017 and mSPCFw overestimate λ by 31-36%, 35-39% and 41-44% respectively. This is consistent with many other traditional classical force fields, which typically overestimate the

thermal conductivity by $\sim$10-50% at temperatures/pressures close to 300 K and 1 bar.[7,134,137–150] Thermal conductivities at 1.00 g cm^{-3} and within 2 K of 300 K have ranged between 0.65-0.91 W K^{-1} m^{-1} for SPC/E[134,139,143,144,148–150] and 0.56-0.91 W K^{-1} m^{-1} for TIP4P/2005[134,148], while extensive NEMD simulations[147] set the thermal conductivities of SPC/E and TIP4P/2005 at temperatures close to 300 K in the range 0.8-0.9 W K^{-1} m^{-1}. Comparing to a dissociative force field, the central force model predicts $\sim$0.63 W K^{-1} m^{-1} at 300 K and 1.00 g cm^{-3},[7] in good agreement with experiment.
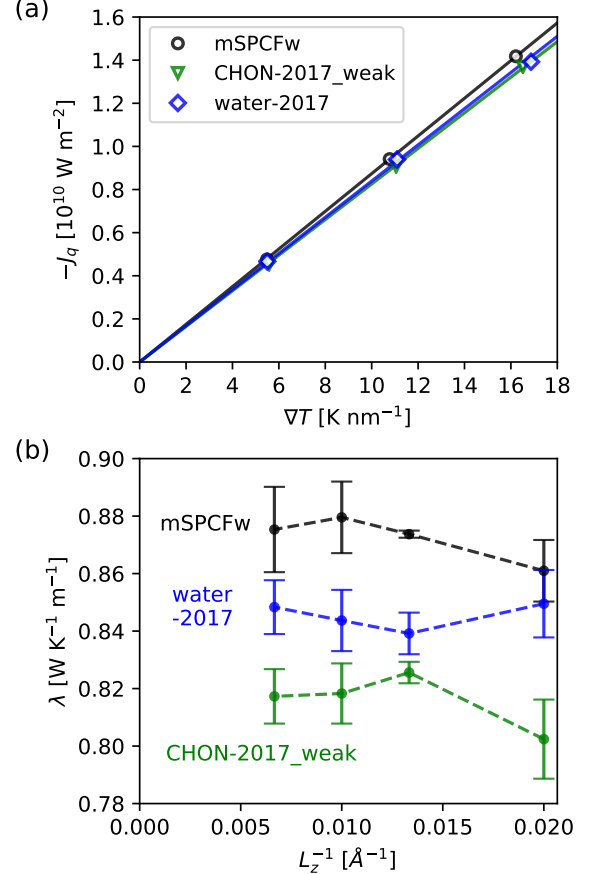

FIG. 16. Thermal conductivity λ at 300 K and 1.00 g cm^{-3}, as predicted by the CHON-2017_weak and water-2017 ReaxFF models, as well as the mSPCFw force field. (a) The linear response of heat flux J_q with local temperature gradient ∇T. Results correspond to $L_z = 75$ Å. Statistical uncertainties (standard error of the mean) are smaller than the symbols. (b) Finite-size analysis: L_z is the length of the simulation cell parallel to the direction of heat flux. For $L_z = 75$ Å, the results corresponding to the linear response fitted in (a) have been plotted.

The largest temperature gradients used in this work approach magnitudes of $\lesssim 20$ K nm^{-1}. This magnitude of thermal gradient is widely used in computer simulations because larger gradients reduce the noise to signal ratio in T, and the statistical uncertainty associated with λ. While experimental setups at the micro and nanoscale are approaching gradients

TABLE VI. Non-equilibrium molecular dynamics simulation parameters and results for the calculation of thermal conductivity λ. L_z is the length of the simulation box parallel to the direction of heat flux. ρ_{box}, T_{box} and P_{zz} are the average density, temperature and pressure parallel to the direction of heat flux, respectively. T_h and T_c are the temperatures of the hot and cold thermostats; ∇T is the resulting temperature gradient. All local properties (columns 8-11) were computed at thermodynamic conditions specified by density ρ and temperature T. Statistical uncertainties in the least significant figure are given in parentheses.

	L_z [Å]	ρ_{box} [g cm^{-3}]	T_c [K]	T_h [K]	T_{box} [K]	P_{zz} [bar]	ρ [g cm^{-3}]	T [K]	∇T [K nm^{-1}]	λ [W K^{-1} m^{-1}]
CHON-2017_weak	50	0.997	287	313	300	152(2)	0.998	300	11.2(2)[a]	0.80(1)
	75	0.997	290	310	300	149(3)	0.998	300	5.6(1)	0.81(2)
	75	0.997	280	320	300	156(2)	0.998	300	11.1(1)	0.82(1)
	75	0.997	270	330	300	164(3)	0.998	300	16.5(1)	0.829(7)
	75	-	-	-	-	-	0.998	300	LR[c]	0.826(4)
	100	0.997	274	326	300	150(2)	0.998	300	10.8(1)	0.82(1)
	150	0.997	280	320	300	153(1)	0.998	300	5.43(6)	0.817(9)
water-2017	50	0.997	287	313	300	−173(2)	0.998	300	11.0(1)[a]	0.85(1)
	75	0.997	290	310	300	−172(2)	0.998	300	5.5(1)	0.85(2)
	75	0.997	280	320	300	−168(3)	0.998	300	11.09(7)	0.847(6)
	75	0.997	270	330	300	−160(3)	0.998	300	16.9(1)	0.826(7)
	75	-	-	-	-	-	0.998	300	LR[c]	0.839(7)
	100	0.997	274	326	300	−176(3)	0.998	300	10.8(1)	0.84(1)
	150	0.997	260	340	300	−141(2)	0.998	300	10.7(1)	0.848(9)
mSPCFw	50	0.997	287	313	300	9(2)	0.998	300	10.6(1)[a]	0.86(1)
	75	0.997	290	310	300	9(3)	0.998	300	5.5(2)	0.87(3)
	75	0.997	280	320	300	14(1)	0.998	300	10.77(8)	0.874(9)
	75	0.997	270	330	300	31(4)	0.999	300	16.2(1)	0.875(9)
	75	-	-	-	-	-	1.00	300	LR[c]	0.873(1)
	100	0.997	285	315	300	0(1)	0.998	300	6.02(8)	0.88(1)
	150	0.997	285	315	300	7(1)	0.998	300	3.98(6)[b]	0.88(1)

[a] A range of ± 5 Å was used when fitting to the temperature profile.
[b] A range of ± 16 Å was used when fitting to the temperature profile.
[c] Linear response (see in text).

of this magnitude[151,152], they are large by macroscopic standards. We show in Fig. 16(a) that all the our results are within the linear regime, and additionally calculate λ_{LR} by fitting the $(\nabla T, J_q)$ data to Fourier's Law.

Finite-size effects are not expected to be significant for the calculated thermal conductivity values, because the thermal transport mechanism in liquid water is dominated by collisions between nearest neighbours, setting a characteristic length scale for heat transport at around one molecular diameter (≈ 3 Å for water). We show in Fig. 16(b) that increasing L_z past 75 Å does not make an appreciable difference; the λ values agree to within their statistical uncertainties.

We note that the thermal conductivities reported in Table VI for the same force field are not expected to be in perfect agreement. This is because they correspond to slightly different thermodynamic conditions, as indicated by the different P_{zz} values. Using the experimental pressure dependence of the thermal conductivity of liquid water along the 300 K isotherm as a guideline, we expect differences $\sim 10^{-3}$ W K^{-1} m^{-1} or less, due to the P_{zz} differences < 40 bar obtained for the same force field. Deviations in λ values are therefore expected to be within their associated uncertainties.

IV. CONCLUSIONS

The rich phenomenology and widescale importance of water continue to motivate the development of computational models that are more accurate, cheaper and/or transferable. ReaxFF models are bond-order based reactive force fields that explicitly include polarization effects through a charge equilibration scheme. They offer an intermediate step between the capabilities of quantum-based electronic structure methods and the computational efficiency of traditional (non-reactive) empirical force fields. One of the key motivations for the development of ReaxFF force fields is the ability to model chemical reactions. Nevertheless, ReaxFF force fields should strive to accurately model both chemical reactivity and thermophysical properties. In this work, we have investigated the performance of two ReaxFF models, CHON-2017_weak and water-2017, in predicting the general thermophysical properties of water. Figure 17 summarizes some of our key results, presenting the deviation of 15 different properties from their experimental values. We close this article with a brief assessment of the ReaxFF models based on our results, and where possible, recommend potential avenues for improvement.

Structure of liquid water. The RFFs reproduce the RDFs of liquid water at near standard conditions reasonably well. They accurately predict the nearest O-O neighbour distance. water-2017 overestimates the height of the first g_{OO} maximum in line with classical force fields such as mSPCFw and
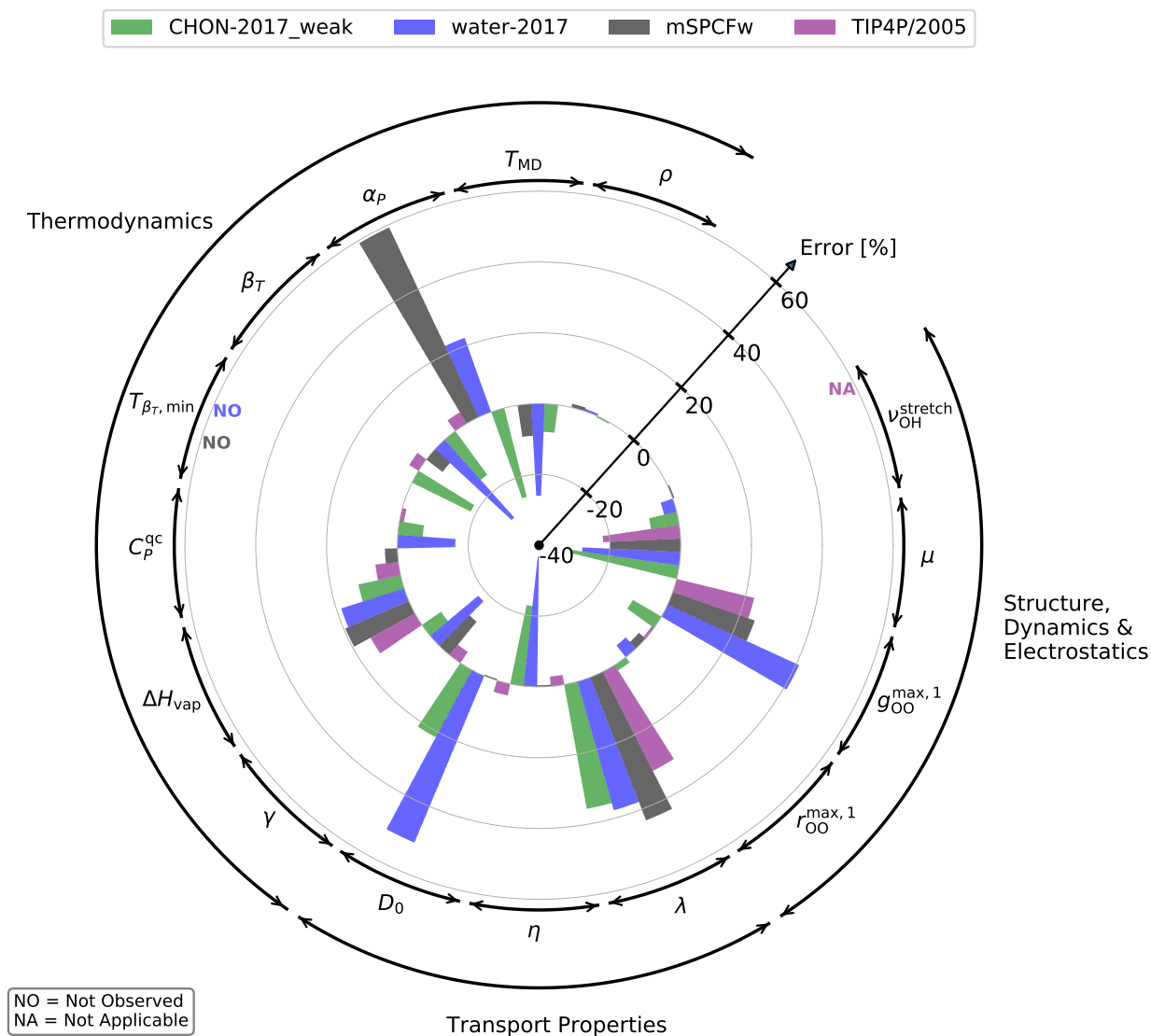
FIG. 17. Deviation from experimental reference values of 15 properties of water predicted by the CHON-2017_weak and water-2017 ReaxFF force fields as well as the classical empirical mSPCFw and TIP4P/2005 force fields. All values correspond to 300 K (where appropriate) and either 1 bar, the vapour pressure for coexistence properties (ΔH_{vap} and γ), or 1.00 g cm^{-3} (see the main text for details). Symbol meanings are given in the main text. Experimental values are from Refs. 45,46,48,51,52,55–57,59 and values for TIP4P/2005 are from Refs. 1,2,66,97,101,121,129,134,147.

TIP4P/2005, while the CHON-2017_weak prediction is in better agreement with the RDFs extracted from neutron and x-ray diffraction experiments. CHON-2017_weak exhibits weaker hydrogen bonding than water-2017, as reflected in a longer hydrogen bonding distance and slightly lower enthalpy of vaporization. Both RFFs possess coordination numbers corresponding to the first (intermolecular) maxima of g_{OO} and g_{OH} in good agreement with experiment.

Vibrational modes and frequencies. The RFF power spectra show good agreement with experiment and empirical flexible force fields in the low frequency region ($<$ 1000 cm^{-1}), with the exception that water-2017 does not possess a shoulder in the oxygen atom power spectrum corresponding to intermolecular stretching vibrations. However, significant deviations from experiment are observed for the intramolecular modes: the O-H stretching frequencies are red-shifted by $\sim$100-300 cm^{-1} and the H-O-H bending frequencies are blue-shifted by $\sim$200-300 cm^{-1}. Furthermore, the RFFs exhibit peak-splitting in the stretching region instead of the single broad peak observed in IR and Raman spectra. This is, at least in part, due to the large differences between gas phase symmetric and asymmetric stretching frequencies. Improving the gas phase frequencies would therefore be the first step in improving the vibrational properties in the liquid phase. Indeed, both RFFs predict gas phase stretching frequencies red-shifted by $\sim$300-500 cm^{-1}, and the water-2017

bending frequency is blue-shifted by ~ 200 cm^{-1}. It is therefore impossible for the RFFs to predict both accurate liquid phase frequencies and shifts from the gas phase, the latter being indicative of hydrogen bonding strength.

Electrostatic moments. Capturing the electrostatic multipole moments of water is essential for building high quality water models, with work[71,72] by Abascal and Vega bringing to light the importance of the quadrupole moment Q_T and ratio μ/Q_T, on top of the dipole moment μ. In the liquid phase, the RFFs predict $\mu = 2.0\text{-}2.2$ D which is substantially lower than the $\mu \sim 2.95$ D expected from experiments[47,48], but only marginally lower than the dipole moments, $\mu =2.3\text{-}2.5$ D of most classical force fields. However, the RFFs have a ratio $\mu/Q_T \approx 1.3$ Å^{-1}, which is significantly higher than the $\mu/Q_T \sim 1.0$ Å^{-1} shown to produce high-quality water models for empirical force fields.[70–72] Improving the μ/Q_T ratio may result in RFFs that predict overall more accurate thermophysical properties. The RFFs predict a shift in dipole moment when going from the liquid to vapour phase of $\Delta_\mathrm{l}^\mathrm{g}\mu = -0.37\text{-}0.39$ D, which is greatly underestimated relative to the $\Delta_\mathrm{l}^\mathrm{g}\mu \sim -1.1$ D expected from experiments[47–50].

Equation of state and thermodynamic response functions. Both RFFs reproduce the density of liquid water at 1 bar fairly accurately. At 300 K, they predict densities to within 1% of the experimental value, and more accurate thermal expansion coefficients than some classical force fields such as mSPCFw (but not TIP4P/2005). Both RFFs feature a density maximum, but greatly underestimate the temperature T_MD at which it occurs: CHON-2017_weak and water-2017 predict (255 ± 3) K and (205 ± 6) K respectively, compared to the 277 K observed experimentally. The isothermal compressibility predicted by the RFFs are systematically lower than experiment, with a more severe underestimation by water-2017. Crucially, our results suggest that CHON-2017_weak possesses a compressibility minimum, albeit at lower temperature of (260 ± 40) K near its T_MD (compared to the experimental 319 K), while water-2017 does not. This suggests that water-2017 is missing aspects of the orientational correlations that are linked to the tetrahedral order of liquid water. The speed of sound predictions are underestimated and largely limited by the RFF's (in)ability to accurately model the compressibility; CHON-2017_weak possesses a maximum while water-2017 does not. Once quantum-corrected, the isobaric and isochoric heat capacities are systematically underestimated, but nonetheless show relatively good agreement with experiment with deviations comparable to many[119–121] classical force fields.

Liquid-vapour coexistence properties. Both RFFs predict orthobaric liquid densities at 300 K in good agreement with experiment, consistent with the density predictions at 300 K and 1 bar. CHON-2017_weak and water-2017 underestimate the surface tension at 300 K by 4-9% and 17-20% respectively. CHON-2017_weak therefore predicts γ in good agreement with experiment: only $\sim 3\%$ lower than TIP4P/2005 and more accurately than many other classical force fields. CHON-2017_weak also predicts more accurate enthalpies of vaporization than water-2017, although both RFFs overestimate ΔH_vap: by 12% and 19% at 300 K for

CHON-2017_weak and water-2017 respectively. These deviations from experiment are in line with TIP4P/2005, SPC/E and mSPCFw, which also overestimate (the uncorrected) ΔH_vap by 10-20%. The greater ΔH_vap of water-2017 suggests that it predicts stronger hydrogen bonding than CHON-2017_weak.

Transport properties. The RFFs overestimate the self-diffusion coefficients and underestimate the viscosity of liquid water at near standard conditions, water-2017 more severely than CHON-2017_weak. This is particularly unfortunate for the water-2017 force field, which was parameterized to model the diffusion of $H_2O/H_3O^+/OH^-$, and included the diffusion coefficients of these species as target parameters for fitting. Presumably, the overestimated self-diffusion coefficient is an artefact that arose from not accounting for finite-size effects in the force field parameterization process. This could be remedied by refitting the force field with the "infinite-size" diffusion coefficients D_0. Likewise, previous estimates[21,25] of the $H_3O^+_\mathrm{(aq)}/OH^-_\mathrm{(aq)}$ diffusion coefficients for both RFFs have not accounted for finite-size effects. Our results for bulk systems indicate that finite-size effects are significant, with the CHON-2017_weak and water-2017 self-diffusion coefficients increasing by $\sim 30\%$ when going from a box length of 12.5 Å to a system of infinite size. These finite-size effects motivate further investigations of the dynamic properties of the RFFs. The thermal conductivity predicted by the RFFs are $\sim 30\text{-}40\%$ higher than the experimental value, in line with popular empirical force fields including TIP4P/2005, SPC/E and mSPCFw.

In conclusion, we have performed comprehensive benchmarks of two state-of-the-art ReaxFF force fields designed to model water, CHON-2017_weak and water-2017, encompassing structural, electrostatic, vibrational, thermodynamic, coexistence, and transport properties. Our results suggest that overall, CHON-2017_weak more accurately predicts the thermophysical properties of water than water-2017. The CHON-2017_weak oxygen and hydrogen atom parameters are used for both water and functionalized hydrocarbons, while water-2017 is a dedicated water force field parameterized to model $H_2O/H_3O^+/OH^-$ diffusion. Comparing to its predecessors[20,22], the description of water by CHON-2017_weak appears to have benefited greatly from the focus on weak interactions in its reparameterization of the protein-2013 force field[22], which included additional training data ranging from the binding energies of water clusters to the chemical reactions of nitrogen containing systems.[23] However, ReaxFF parameters are highly correlated, and dedicated water force fields such as water-2017 should be able to sacrifice transferability for accuracy. Our results suggest that improving the μ/Q_T ratio, self-diffusion coefficients and gas phase frequencies are first steps towards building ReaxFF models that more accurately describe the thermophysical properties of liquid water. This could be achieved by including these quantities as target parameters in the force field optimization procedure.

TABLE VII. mSPCFw force field parameters. E_p is the potential energy.

Partial atomic charges:	$E_P^{\text{Coulomb}}(r_{ij}) = q_i q_j/(4\pi\varepsilon_0 r_{ij})$	
q_O [e]	-0.82	
q_H [e]	0.41	
Lennard-Jones potential:	$E_P^{\text{LJ}}(r) = 4\varepsilon[(\sigma/r)^{12} - (\sigma/r)^6]$	
ε_{OO} [kcal mol^{-1}]	0.1554253	
σ_{OO} [Å]	3.165492	
Morse potential (O-H bond):	$E_P^{\text{bond}}(r) = D_0^{\text{bond}}(e^{-2a(r-r_0)} - 2e^{-a(r-r_0)})$	
D_0^{bond} [kcal mol^{-1}]	117.6549	
r_0 [Å]	1.012	
a [Å^{-1}]	2.1578	
Harmonic potential (H-O-H angle):	$E_P^{\text{bend}}(\theta) = k_a(\theta - \theta_0)^2/2$	
k_a [kcal mol^{-1} rad^{-2}]	101.3742	
θ_0 [°]	113.24	

ACKNOWLEDGMENTS

DATA AVAILABILITY

The data that supports the findings of this study are available from the corresponding author upon reasonable request.

Appendix A: The mSPCFw force field for water

The modified SPC flexible (mSPCFw) model[5] is a three-centre, flexible and non-polarizable force field based on the flexible SPC (SPCFw) water model[4] of Wu *et al.*. It shares the same intermolecular potentials but replaces the harmonic O-H bond potential with a Morse potential, and adjusts the bending potential to mimic the vibrational frequencies of an isolated H_2O molecule.[5]

The force field parameters used in this work are shown in Table VII. The intermolecular potentials were taken directly from Ref. 4, while the new intramolecular parameters were taken from Ref. 5. Where units have been converted, they have been stated to 7 significant figures, as is consistent with the level of precision given in Ref. 4 for the Lennard-Jones parameters.

[1] C. Vega and J. L. F. Abascal, "Simulating water with rigid non-polarizable models: a general perspective," Phys. Chem. Chem. Phys. **13**, 19663–19688 (2011).

[2] J. L. F. Abascal and C. Vega, "A general purpose model for the condensed phases of water: Tip4p/2005," J. Chem. Phys. **123**, 234505 (2005).

[3] H. J. C. Berendsen, J. R. Grigera, and T. P. Straatsma, "The missing term in effective pair potentials," J. Phys. Chem. **91**, 6269–6271 (1987).

[4] T. Wu, H. L. Tepper, and G. A. Voth, "Flexible simple point-charge water model with improved liquid-state properties," J. Chem. Phys. **124**, 024503 (2006).

[5] K. S. Smirnov, "A molecular dynamics study of the interaction of water with the external surface of silicalite-1," Phys. Chem. Chem. Phys. **19**, 2950–2960 (2017).

[6] H. L. Lemberg and F. H. Stillinger, "Central-force model for liquid water," The Journal of Chemical Physics **62**, 1677–1690 (1975), https://doi.org/10.1063/1.430718.

[7] F. Bresme, "Equilibrium and nonequilibrium molecular-dynamics simulations of the central force model of water," J. Chem. Phys. **115**, 7564–7574 (2001).

[8] Z. Jing, C. Liu, S. Y. Cheng, R. Qi, B. D. Walker, J.-P. Piquemal, and P. Ren, "Polarizable force fields for biomolecular simulations: Recent advances and applications," Annu. Rev. Biophys **48**, 371–394 (2019).

[9] A. A. Chialvo and P. T. Cummings, "Engineering a simple polarizable model for the molecular simulation of water applicable over wide ranges of state conditions," The Journal of Chemical Physics **105**, 8274–8281 (1996), https://doi.org/10.1063/1.472718.

[10] P. Ren and J. W. Ponder, "Polarizable atomic multipole water model for molecular mechanics simulation," *The Journal of Physical Chemistry B*, The Journal of Physical Chemistry B **107**, 5933–5947 (2003).

[11] P. Paricaud, M. Předota, A. A. Chialvo, and P. T. Cummings, "From dimer to condensed phases at extreme conditions: Accurate predictions of the properties of water by a gaussian charge polarizable model," The Journal of Chemical Physics **122**, 244511 (2005), https://doi.org/10.1063/1.1940033.

[12] G. A. Cisneros, K. T. Wikfeldt, L. Ojamäe, J. Lu, Y. Xu, H. Torabifard, A. P. Bartók, G. Csányi, V. Molinero, and F. Paesani, "Modeling molecular interactions in water: From pairwise to many-body potential energy functions," Chem. Rev. **116**, 7501–7528 (2016).

[13] V. Molinero and E. B. Moore, "Water modeled as an intermediate element between carbon and silicon," *The Journal of Physical Chemistry B*, The Journal of Physical Chemistry B **113**, 4008–4016 (2009).

[14] M. J. Gillan, D. Alfè, and A. Michaelides, "Perspective: How good is dft for water?" J. Chem. Phys. **144**, 130901 (2016).

[15] A. P. Gaiduk, F. Gygi, and G. Galli, "Density and compressibility of liquid water and ice from first-principles simulations with hybrid functionals," J. Phys. Chem. Lett. **6**, 2902–2908 (2015).

[16] M. Chen, H.-Y. Ko, R. C. Remsing, M. F. Calegari Andrade, B. Santra, Z. Sun, A. Selloni, R. Car, M. L. Klein, J. P. Perdew, and X. Wu, "Ab initio theory and modeling of water," Proc. Natl. Acad. Sci. U. S. A. **114**, 10846–10851 (2017).

[17] B. Chen, I. Ivanov, M. L. Klein, and M. Parrinello, "Hydrogen bonding in water," Phys. Rev. Lett. **91**, 215503 (2003).

[18] L. Ruiz Pestana, N. Mardirossian, M. Head-Gordon, and T. Head-Gordon, "Ab initio molecular dynamics simulations of liquid water using high quality meta-gga functionals," Chem. Sci. **8**, 3554–3565 (2017).

[19] G. Zhao, S. Shi, H. Xie, Q. Xu, M. Ding, X. Zhao, J. Yan, and D. Wang, "Equation of state of water based on the scan meta-gga density functional," Phys. Chem. Chem. Phys. **22**, 4626–4631 (2020).

[20] A. C. T. van Duin, C. Zou, K. Joshi, V. Bryantsev, and W. A. Goddard, "Computational catalysis," (The Royal Society of Chemistry, Thomas Graham House, Science Park, Milton Road, Cambridge CB4 0WF, UK, 2013) Chap. 6, pp. 223–243.

[21] W. Zhang and A. C. T. van Duin, "Second-generation reaxff water force field: Improvements in the description of water density and oh-anion diffusion," J. Phys. Chem. B **121**, 6021–6032 (2017).

[22] S. Monti, A. Corozzi, P. Fristrup, K. L. Joshi, Y. K. Shin, P. Oelschlaeger, A. C. T. van Duin, and V. Barone, "Exploring the conformational and reactive dynamics of biomolecules in solution using an extended version of the glycine reactive force field," Phys. Chem. Chem. Phys. **15**, 15062–15077 (2013).

[23] W. Zhang and A. C. T. van Duin, "Improvement of the reaxff description

for functionalized hydrocarbon/water weak interactions in the condensed phase," J. Phys. Chem. B **122**, 4083–4092 (2018).

[24]L. Ai, Y. Zhou, and M. Chen, "A reactive force field molecular dynamics simulation of the dynamic properties of hydrogen bonding in supercritical water," J. Mol. Liq. **276**, 83–92 (2019).

[25]W. Zhang, X. Chen, and A. C. T. van Duin, "Isotope effects in water: Differences of structure, dynamics, spectrum, and proton transport between heavy and light water from reaxff reactive force field simulations," J. Phys. Chem. Lett. **9**, 5445–5452 (2018).

[26]P. Saidi, L. K. Béland, and M. R. Daymond, "Graphene oxide membranes for water isotope filtration: Insight at the nano- and microscale," J. Phys. Chem. C **124**, 26864–26873 (2020).

[27]L. Shi, A. Xu, and Y. Cheng, "Ether-group-mediated aqueous proton selective transfer across graphene-embedded 18-crown-6 ether pores," J. Phys. Chem. C **123**, 27429–27435 (2019).

[28]L. Shi, Z. Ying, A. Xu, and Y. Cheng, "Unraveling the water-mediated proton conduction mechanism along the surface of graphene oxide," Chem. Mater. **32**, 6062–6069 (2020).

[29]B. R. H. de Aquino, H. Ghorbanfekr-Kalashami, M. Neek-Amal, and F. M. Peeters, "Ionized water confined in graphene nanochannels," Phys. Chem. Chem. Phys. **21**, 9285–9295 (2019).

[30]D. Dong, W. Zhang, A. C. T. van Duin, and D. Bedrov, "Grotthuss versus vehicular transport of hydroxide in anion-exchange membranes: Insight from combined reactive and nonreactive molecular simulations," J. Phys. Chem. Lett. **9**, 825–829 (2018).

[31]W. Zhang, D. Dong, D. Bedrov, and A. C. T. van Duin, "Hydroxide transport and chemical degradation in anion exchange membranes: a combined reactive and non-reactive molecular simulation study," J. Mater. Chem. A **7**, 5442–5452 (2019).

[32]N. Dasgupta, D. E. Yilmaz, and A. van Duin, "Simulations of the biodegradation of citrate-based polymers for artificial scaffolds using accelerated reactive molecular dynamics," J. Phys. Chem. B **124**, 5311–5322 (2020).

[33]H. Manzano, W. Zhang, M. Raju, J. S. Dolado, I. n. López-Arbeloa, and A. C. T. van Duin, "Benchmark of reaxff force field for subcritical and supercritical water," J. Chem. Phys. **148**, 234503 (2018).

[34]I. Leven, H. Hao, A. K. Das, and T. Head-Gordon, "A reactive force field with coarse-grained electrons for liquid water," J. Phys. Chem. Lett. **11**, 9240–9247 (2020).

[35]K. Heijmans, I. C. Tranca, D. M. J. Smeulders, T. J. H. Vlugt, and S. V. Gaastra-Nedea, "Gibbs ensemble monte carlo for reactive force fields to determine the vapor–liquid equilibrium of co2 and h2o," J. Chem. Theory Comput. **17**, 322–329 (2021).

[36]A. C. T. van Duin, S. Dasgupta, F. Lorant, and W. A. Goddard III, "Reaxff: A reactive force field for hydrocarbons," J. Phys. Chem. A **105**, 9396–9409 (2001).

[37]W. J. Mortier, S. K. Ghosh, and S. Shankar, "Electronegativity-equalization method for the calculation of atomic charges in molecules," J. Am. Chem. Soc. **108**, 4315–4320 (1986).

[38]H. M. Aktulga, J. C. Fogart, S. A. Pandit, and A. Y. Grama, "Parallel reactive molecular dynamics: Numerical methods and algorithmic techniques," Parallel Computing **38**, 245–259 (2012).

[39]T. P. Senftle, S. Hong, M. M. Islam, S. B. Sylasa, Y. Zheng, Y. K. Shin, C. Junkermeier, R. Engel-Herbert, M. J. Janik, H. M. Aktulga, T. Verstraelen, A. Grama, and A. C. T. van Duin, "The reaxff reactive force-field: development, applications and future directions," npj Comput. Mater. **2**, 15011 (2016).

[40]S. Plimpton, "Fast parallel algorithms for short-range molecular dynamics," J. Comput. Phys. **117**, 1–19 (1995).

[41]D. Furman and D. J. Wales, "Transforming the accuracy and numerical stability of reaxff reactive force fields," J. Phys. Chem. Lett. **10**, 7215–7223 (2019).

[42]D. Furman and D. J. Wales, "A well-behaved theoretical framework for reaxff reactive force fields," J. Chem. Phys. **153**, 021102 (2020).

[43]E. Pollock and J. Glosli, "Comments on p3m, fmm, and the ewald method for large periodic coulombic systems," Comput. Phys. Commun. **95**, 93–110 (1996).

[44]M. Allen and D. Tildesley, *Computer Simulation of Liquids* (Oxford: Clarendon Pr, 1987).

[45]W. Wagner and A. Pruß, "The iapws formulation 1995 for the thermo-dynamic properties of ordinary water substance for general and scientific use," J. Phys. Chem. Ref. Data **31**, 387–535 (2002).

[46]L. B. Skinner, C. Huang, D. Schlesinger, L. G. M. Pettersson, A. Nilsson, and C. J. Benmore, "Benchmark oxygen-oxygen pair-distribution function of ambient water from x-ray diffraction measurements with a wide q-range," J. Chem. Phys. **138**, 074506 (2013).

[47]Y. S. Badyal, M.-L. Saboungi, D. L. Price, S. D. Shastri, D. R. Haeffner, and A. K. Soper, "Electron distribution in water," J. Chem. Phys. **112**, 9206–9208 (2000).

[48]A. V. Gubskaya and P. G. Kusalik, "The total molecular dipole moment for liquid water," J. Chem. Phys. **117**, 5290–5302 (2002).

[49]S. A. Clough, Y. Beers, G. P. Klein, and L. S. Rothman, "Dipole moment of water from stark measurements of h2o, hdo, and d2o," The Journal of Chemical Physics **59**, 2254–2259 (1973).

[50]S. L. Shostak, W. L. Ebenstein, and J. S. Muenter, "The dipole moment of water. i. dipole moments and hyperfine properties of h2o and hdo in the ground and excited vibrational states," J. Chem. Phys. **94**, 5875 (1991).

[51]C. Chapados and J.-J. Max, "Isotope effects in liquid water by infrared spectroscopy. iii. h2o and d2o spectra from 6000 to 0 cm^{-1}," J. Chem. Phys. **131**, 184505 (2009).

[52]S. Y. Venyaminov and F. G. Prendergast, "Water (h2o and d2o) molar absorptivity in the 1000-4000 cm^{-1} range and quantitative infrared spectroscopy of aqueous solutions," Anal. Biochem. **248**, 234–245 (1997).

[53]D. M. Carey and G. M. Korenowski, "Measurement of the raman spectrum of liquid water," J. Chem. Phys. **108**, 2669–2675 (1998).

[54]G. E. Walrafen, "Raman spectral studies of water structure," J. Chem. Phys. **40**, 3249–3256 (1964).

[55]M. Holz, S. R. Heil, and A. Sacco, "Temperature-dependent self-diffusion coefficients of water and six selected molecular liquids for calibration in accurate ^{1}h nmr pfg measurements," Phys. Chem. Chem. Phys. **2**, 4740–4742 (2000).

[56]M. L. Huber, R. A. Perkins, A. Laesecke, D. G. Friend, J. V. Sengers, M. J. Assael, I. N. Metaxa, E. Vogel, R. Mareš, and K. Miyagawa, "New international formulation for the viscosity of h2o," J. Phys. Chem. Ref. Data **38**, 101–125 (2000).

[57]M. L. Huber, R. A. Perkins, D. G. Friend, J. V. Sengers, M. J. Assael, I. N. Metaxa, K. Miyagawa, R. Hellmann, and E. Vogel, "New international formulation for the thermal conductivity of h2o," J. Chem. Phys. Ref. Data **41**, 033102 (2012).

[58]I. A. for the Properties of Water and Steam, "Uncertainties in enthalpy for the iapws formulation 1995 for the thermodynamic properties of ordinary water substance for general and scientific use (iapws-95) and the iapws industrial formulation 1997 for the thermodynamic properties of water and steam (iapws-if97)," IAPWS AN1-03 (2003).

[59]N. B. Vargaftik, B. N. Volkov, and L. D. Voljak, "International tables of the surface tension of water," J. Phys. Chem. Ref. Data **12**, 817–820 (1983).

[60]A. K. Soper and C. J. Benmore, "Quantum differences between heavy and light water," Phys. Rev. Lett. **101**, 065502 (2008).

[61]M. Ceriotti, W. Fang, P. G. Kusalik, R. H. McKenzie, A. Michaelides, M. A. Morales, and T. E. Markland, "Nuclear quantum effects in water and aqueous systems: Experiment, theory, and current challenges," Chem. Rev. **116**, 7529–7550 (2016).

[62]A. K. Soper, "The radial distribution functions of water and ice from 220 to 673 k and at pressures up to 400 mpa," Chem. Phys. **258**, 121–137 (2000).

[63]L. B. Skinner, C. J. Benmore, J. C. Neuefeind, and J. B. Parise, "The structure of water around the compressibility minimum," J. Chem. Phys. **141**, 214507 (2014).

[64]C. Benmore, L. C. Gallington, and E. Soignard, "Intermediate range order in supercooled water," Mol. Phys. **117**, 2470–2476 (2019).

[65]H. Pathak, A. Späh, K. H. Kim, I. Tsironi, D. Mariedahl, M. Blanco, S. Huotari, V. Honkimäki, and A. Nilsson, "Intermediate range o–o correlations in supercooled water down to 235 k," J. Chem. Phys. **150**, 224506 (2019).

[66]G. Camisasca, H. Pathak, K. T. Wikfeldt, and L. G. M. Pettersson, "Radial distribution functions of water: Models vs experiments," J. Chem. Phys. **151**, 044502 (2019).

[67]C. Apostolidou, "Oh radical in water from ab initio molecular dynamics simulation employing hybrid functionals," J. Chem. Phys. **151**, 064111 (2019).

[68]S. K. Reddy, S. C. Straight, P. Bajaj, C. Huy Pham, M. Riera, D. R.

Moberg, M. A. Morales, C. Knight, A. W. Götz, and F. Paesani, "On the accuracy of the mb-pol many-body potential for water: Interaction energies, vibrational frequencies, and classical thermodynamic and dynamical properties from clusters to liquid water and ice," J. Chem. Phys. **145**, 194504 (2016).

[69] J. Verhoeven and A. Dymanus, "Magnetic properties and molecular quadrupole tensor of the water molecule by beam-maser zeeman spectroscopy," J. Chem. Phys. **52**, 3222–3233 (1970).

[70] S. Izadi, R. Anandakrishnan, and A. V. Onufriev, "Building water models: A different approach," J. Phys. Chem. Lett. **5**, 3863–3871 (2014).

[71] J. L. F. Abascal and C. Vega, "Dipole-quadrupole force ratios determine the ability of potential models to describe the phase diagram of water," Phys. Rev. Lett. **98**, 237801 (2007).

[72] J. L. F. Abascal and C. Vega, "The water forcefield: importance of dipolar and quadrupolar interactions," J. Phys. Chem. C **111**, 15811–15822 (2007).

[73] C. Zhang, J. Wu, G. Galli, and F. Gygi, "Structural and vibrational properties of liquid water from van der waals density functionals," J. Chem. Theory Comput. **7**, 3054–3061 (2011).

[74] L. Zheng, M. Chen, Z. Sun, H.-Y. Ko, B. Santra, P. Dhuvad, and X. Wu, "Structural, electronic, and dynamical properties of liquid water by ab initio molecular dynamics based on scan functional within the canonical ensemble," J. Chem. Phys. **148**, 164505 (2018).

[75] F. Martin and H. Zipse, "Charge distribution in the water molecule—a comparison of methods," Journal of Computational Chemistry **26**, 97–105 (2005).

[76] B. Han, C. M. Isborn, and L. Shi, "Determining partial atomic charges for liquid water: Assessing electronic structure and charge models," J. Chem. Theory Comput. **17**, 889–901 (2021).

[77] H. J. Bakker and J. L. Skinner, "Vibrational spectroscopy as a probe of structure and dynamics in liquid water," Chem. Rev. **110**, 1498–1517 (2010).

[78] F. Perakis, L. De Marco, A. Shalit, F. Tang, Z. R. Kann, T. D. Kühne, R. Torre, M. Bonn, and Y. Nagata, "Vibrational spectroscopy and dynamics of water," Chem. Rev. **116**, 7590–7607 (2016).

[79] K. M. Hunter, F. A. Shakib, and F. Paesani, "Disentangling coupling effects in the infrared spectra of liquid water," J. Phys. Chem. B. **122**, 10754–10761 (2018).

[80] C.-C. Yu, K.-Y. Chiang, M. Okuno, T. Seki, T. Ohto, X. Yu, V. Korepanov, H.-o. Hamaguchi, M. Bonn, J. Hunger, and Y. Nagata, "Vibrational couplings and energy transfer pathways of water's bending mode," Nat. Commun. **11**, 5977 (2020).

[81] G. R. Medders and F. Paesani, "Infrared and raman spectroscopy of liquid water through "first-principles" many-body molecular dynamics," J. Chem. Theory Comput. **11**, 1145–1154 (2015).

[82] P. Bopp, G. Jancsó, and K. Heinzinger, "An improved potential for nonrigid water molecules in the liquid phase," Chemical Physics Letters **98**, 129–133 (1983).

[83] W. S. Benedict, N. Gailar, and E. K. Plyler, "Rotation-vibration spectra of deuterated water vapor," J. Chem. Phys. **24**, 1139–1165 (1956).

[84] R. Rey, K. B. Møller, and J. T. Hynes, "Hydrogen bond dynamics in water and ultrafast infrared spectroscopy," J. Phys. Chem. A. **106**, 11993–11996 (2002).

[85] D. Ojha, K. Karhan, and T. D. Kühne, "On the hydrogen bond strength and vibrational spectroscopy of liquid water," Sci. Rep. **8**, 16888 (2018).

[86] M. Falk, "The frequency of the h-o-h bending fundamental in solids and liquids," Spectrochim. Acta **40**, 43–48 (1984).

[87] M. A. González and J. L. F. Abascal, "A flexible model for water based on tip4p/2005," The Journal of Chemical Physics **135**, 224516 (2011).

[88] J. Martí, J. A. Padro, and E. Guàrdia, "Molecular dynamics simulation of liquid water along the coexistence curve: Hydrogen bonds and vibrational spectra," J. Chem. Phys. **105**, 639–649 (1996).

[89] O. V. Boyarkin, M. A. Koshelev, O. Aseev, P. Maksyutenko, T. R. Rizzo, N. F. Zobov, L. Lodi, J. Tennyson, and O. L. Polyansky, "Accurate bond dissociation energy of water determined by triple-resonance vibrational spectroscopy and ab initio calculations," Chem. Phys. Lett. **568-569**, 14–20 (2013).

[90] U. W. Schmitt and G. A. Voth, "The computer simulation of proton transport in water," J. Chem. Phys. **111**, 9361–9381 (1999).

[91] L. X. Dang and B. M. Pettitt, "Simple intramolecular model potentials for

[92] B. E. Rocher-Casterline, L. C. Ch'ng, A. K. Mollner, and H. Reisler, "Communication: Determination of the bond dissociation energy (d0) of the water dimer, (h2o)2, by velocity map imaging," The Journal of Chemical Physics **134**, 211101 (2011).

[93] N. A. Benedek, I. K. Snook, M. D. Towler, and R. J. Needs, "Quantum monte carlo calculations of the dissociation energy of the water dimer," The Journal of Chemical Physics **125**, 104302 (2006).

[94] I. G. Gurtubay and R. J. Needs, "Dissociation energy of the water dimer from quantum monte carlo calculations," The Journal of Chemical Physics **127**, 124306 (2007).

[95] A. Mukhopadhyay, S. S. Xantheas, and R. J. Saykally, "The water dimer ii: Theoretical investigations," Chemical Physics Letters **700**, 163–175 (2018).

[96] L.-P. Wang, T. J. Martinez, and V. S. Pande, "Building force fields: An automatic, systematic, and reproducible approach," J. Phys. Chem. Lett. **5**, 1885–1891 (2014).

[97] H. L. Pi, J. L. Aragones, C. Vega, E. G. Noya, J. L. F. Abascal, M. A. Gonzalez, and C. McBride, "Anomalies in water as obtained from computer simulations of the tip4p/2005 model: density maxima, and density, isothermal compressibility and heat capacity minima," Mol. Phys. **107**, 365–374 (2009).

[98] D. Paschek, "Temperature dependence of the hydrophobic hydration and interaction of simple solutes: An examination of five popular water models," J. Chem. Phys. **120**, 6674–6690 (2004).

[99] H. W. Horn, W. C. Swope, J. W. Pitera, J. D. Madura, T. J. Dick, G. L. Hura, and T. Head-Gordon, "Development of an improved four-site water model for biomolecular simulations: Tip4p-ew," J. Phys. Chem. **120**, 9665 (2004).

[100] A. W. Milne and M. Jorge, "Polarization corrections and the hydration free energy of water," J. Chem. Theory Comput. **15**, 1065–1078 (2019).

[101] J. Alejandre and G. A. Chapela, "The surface tension of tip4p/2005 water model using the ewald sums for the dispersion interactions," J. Chem. Phys. **132**, 014701 (2010).

[102] C. Vega and E. de Miguel, "Surface tension of the most popular models of water by using the test-area simulation method," J. Chem. Phys. **126**, 154707 (2007).

[103] R. D. Mountain, "An internally consistent method for the molecular dynamics simulation of the surface tension: Application to some tip4p-type models of water," J. Phys. Chem. B **113**, 482–486 (2009).

[104] P. K. Yuet and D. Blankschtein, "Molecular dynamics simulation study of water surfaces: Comparison of flexible water models," J. Phys. Chem. B **114**, 13786–13795 (2010).

[105] A. Ghoufi and P. Malfreyt, "Calculation of the surface tension of water: 40 years of molecular simulations," Mol. Simul. **45**, 295–303 (2019).

[106] C. Huang, K. T. Wikfeldt, D. Nordlund, U. Bergmann, T. McQueen, J. Sellberg, L. G. M. Pettersson, and A. Nilsson, "Wide-angle x-ray diffraction and molecular dynamics study of medium-range order in ambient and hot water," Phys. Chem. Chem. Phys. **13**, 19997–20007 (2011).

[107] D. Schlesinger, K. T. Wikfeldt, L. B. Skinner, C. J. Benmore, A. Nilsson, and L. G. M. Pettersson, "The temperature dependence of intermediate range oxygen-oxygen correlations in liquid water," J. Chem. Phys. **145**, 084503 (2016).

[108] A. Nilsson and L. G. M. Pettersson, "The structural origin of anomalous properties of liquid water," Nature Communications **6**, 8998 (2015).

[109] J. Russo and H. Tanaka, "Understanding water's anomalies with locally favoured structures," Nature Communications **5**, 3556 (2014).

[110] M. Vedamuthu, S. Singh, and G. W. Robinson, "Properties of liquid water. 4. the isothermal compressibility minimum near 50 .degree.c," J. Phys. Chem. **99**, 9263–9267 (1995).

[111] R. S. Singh, J. W. Biddle, P. G. Debenedetti, and M. A. Anisimov, "Two-state thermodynamics and the possibility of a liquid-liquid phase transition in supercooled tip4p/2005 water," The Journal of Chemical Physics **144**, 144504 (2016), https://doi.org/10.1063/1.4944986.

[112] A. K. Soper and M. A. Ricci, "Structures of high-density and low-density water," Phys. Rev. Lett. **84**, 2881–2884 (2000).

[113] M. Nakamura, K. Tamura, and S. Murakami, "Isotope effects on thermodynamic properties: mixtures of x(d2o or h2o) + (1 x)ch3cn at 298.15 k," Thermochim. Acta **253**, 127–136 (1995).

[114] C. Vega, M. M. Conde, C. McBride, J. L. F. Abascal, E. G. Noya,

R. Ramirez, and L. M. Sesé, "Heat capacity of water: A signature of nuclear quantum effects," J. Chem. Phys. **132**, 046101 (2010).

[115] P. H. Berens, D. H. J. Mackay, G. M. White, and K. R. Wilson, "Thermodynamics and quantum corrections from molecular dynamics for liquid water," J. Chem. Phys **79**, 2375–2389 (1983).

[116] S.-T. Lin, M. Blanco, and W. A. Goddard, "The two-phase model for calculating thermodynamic properties of liquids from molecular dynamics: Validation for the phase diagram of lennard-jones fluids," J. Chem. Phys. **119**, 11792–11805 (2003).

[117] S.-T. Lin, P. K. Maiti, and W. A. Goddard, "Two-phase thermodynamic model for efficient and accurate absolute entropy of water from molecular dynamics simulations," J. Phys. Chem. B **114**, 8191–8198 (2010).

[118] T. A. Pascal, S.-T. Lin, and W. A. Goddard III, "Thermodynamics of liquids: standard molar entropies and heat capacities of common solvents from 2pt molecular dynamics," Phys. Chem. Chem. Phys. **13**, 169–181 (2011).

[119] D. Berta, D. Ferenc, I. Bakó, and Madarász, "Nuclear quantum effects from the analysis of smoothed trajectories: Pilot study for water," J. Chem. Theory Comput. **16**, 3316–3334 (2020).

[120] Q. Waheed and O. Edholm, "Quantum corrections to classical molecular dynamics simulations of water and ice," J. Chem. Theory Comput. **7**, 2903–2909 (2011).

[121] T. A. Pascal, D. Schärf, Y. Jung, and T. D. Kühne, "On the absolute thermodynamics of water from computer simulations: A comparison of first-principles molecular dynamics, reactive and empirical force fields," J. Chem. Phys. **137**, 244507 (2012).

[122] K.-Y. Yeh, S.-N. Huang, L.-J. Chen, and S.-T. Lin, "Diffusive and quantum effects of water properties in different states of matter," J. Chem. Phys. **141**, 044502 (2014).

[123] M. A. Caro, O. Lopez-Acevedo, and T. Laurila, "Redox potentials from ab initio molecular dynamics and explicit entropy calculations: Application to transition metals in aqueous solution," J. Chem. Theory Comput. **13**, 3432–3441 (2017).

[124] F. Bresme, J. W. Biddle, J. V. Sengers, and M. A. Anisimov, "Communication: Minimum in the thermal conductivity of supercooled water: A computer simulation study," J. Chem. Phys. **140**, 161104 (2014).

[125] V. Holten, J. V. Sengers, and M. A. Anisimov, "Equation of state for supercooled water at pressures up to 400 mpa," J. Phys. Chem. Ref. Data **43**, 043101 (2014).

[126] I.-C. Yeh and G. Hummer, "System-size dependence of diffusion coefficients and viscosities from molecular dynamics simulations with periodic boundary conditions," J. Phys. Chem. B **108**, 15873–15879 (2004).

[127] B. Dünweg and K. Kremer, "Molecular dynamics simulation of a polymer chain in solution," J. Chem. Phys. **99**, 6983–6997 (1993).

[128] R. Mills, "Self-diffusion in normal and heavy water in the range 1-45.deg." J. Phys. Chem. **77**, 685–688 (1973).

[129] S. Tazi, A. Boţan, M. Salanne, V. Marry, P. Turq, and B. Rotenberg, "Diffusion coefficient and shear viscosity of rigid water models," J. Phys.: Condens. Matter **24**, 284117 (2012).

[130] T. D. Kühne, M. Krack, and M. Parrinello, "Static and dynamical properties of liquid water from first principles by a novel carparrinello-like approach," J. Chem. Theory Comput. **5**, 235–241 (2009).

[131] J. E. Basconi and M. R. Shirts, "Effects of temperature control algorithms on transport properties and kinetics in molecular dynamics simulations," J. Chem. Theory Comput. **9**, 2887–2899 (2013).

[132] T. S. Light, S. Licht, A. C. Bevilacqua, and K. R. Morash, "The fundamental conductivity and resistivity of water," Electrochemical and Solid-State Letters **8**, E16 (2005).

[133] M. A. González and J. L. F. Abascal, "The shear viscosity of rigid water models," J. Chem. Phys. **132**, 096101 (2010).

[134] S. H. Lee and J. Kim, "Transport properties of bulk water at 243–550 k: a comparative molecular dynamics simulation study using spc/e, tip4p, and tip4p/2005 water models," Mol. Phys. **117**, 1926–1933 (2019).

[135] F. Bresme, A. Lervik, D. Bedeaux, and S. Kjelstrup, "Water polarization under thermal gradients," Phys. Rev. Lett. **101**, 020602 (2008).

[136] O. R. Gittus, P. Albella, and F. Bresme, "Polarization of acetonitrile under thermal fields via non-equilibrium molecular dynamics simulations," J. Chem. Phys. **153**, 204503 (2020).

[137] T. Ohara, "Intermolecular energy transfer in liquid water and its contribution to heat conduction: A molecular dynamics study," J. Chem. Phys. **111**, 6492–6500 (1999).

[138] D. Bedrov and G. D. Smith, "Thermal conductivity of molecular fluids from molecular dynamics simulations: Application of a new imposed-flux method," J. Chem. Phys. **113**, 8080–8084 (2000).

[139] M. Zhang, E. Lussetti, L. E. S. de Souza, and F. Müller-Plathe, "Thermal conductivities of molecular liquids by reverse nonequilibrium molecular dynamics," J. Phys. Chem. B **109**, 15060–15067 (2005).

[140] T. Terao and F. Müller-Plathe, "A nonequilibrium molecular dynamics method for thermal conductivities based on thermal noise," J. Chem. Phys. **122**, 081103 (2005).

[141] W. Evans, J. Fish, and P. Keblinski, "Thermal conductivity of ordered molecular water," J. Chem. Phys. **126**, 154504 (2007).

[142] E. J. Rosenbaum, N. J. English, J. K. Johnson, D. W. Shaw, and R. P. Warzinski, "Thermal conductivity of methane hydrate from experiment and molecular simulation," J. Phys. Chem. B **111**, 13194–13205 (2007).

[143] H. Jiang, E. M. Myshakin, K. D. Jordan, and R. P. Warzinski, "Molecular dynamics simulations of the thermal conductivity of methane hydrate," J. Phys. Chem. B **112**, 10207–10216 (2008).

[144] S. Kuang and J. D. Gezelter, "A gentler approach to rnemd: Nonisotropic velocity scaling for computing thermal conductivity and shear viscosity," J. Chem. Phys. **133**, 164101 (2010).

[145] J. Muscatello and F. Bresme, "A comparison of coulombic interaction methods in non-equilibrium studies of heat transfer in water," J. Chem. Phys. **135**, 234111 (2011).

[146] J. Muscatello, F. Römer, J. Sala, and F. Bresme, "Water under temperature gradients: polarization effects and microscopic mechanisms of heat transfer," Phys. Chem. Chem. Phys. **13**, 19970–19978 (2011).

[147] F. Römer, A. Lervik, and F. Bresme, "Nonequilibrium molecular dynamics simulations of the thermal conductivity of water: A systematic investigation of the spc/e and tip4p/2005 models," J. Chem. Phys. **137**, 074503 (2012).

[148] Y. Mao and Y. Zhang, "Thermal conductivity, shear viscosity and specific heat of rigid water models," Chem. Phys. Lett. **542**, 37–41 (2012).

[149] T. W. Sirk, S. Moore, and E. F. Brown, "Characteristics of thermal conductivity in classical water models," J. Chem. Phys. **138**, 064505 (2013).

[150] S. H. Lee, "Temperature dependence of the thermal conductivity of water: a molecular dynamics simulation study using the spc/e model," Mol. Phys. **112**, 2155–2159 (2014).

[151] A. O. Govorov, W. Zhang, T. Skeini, H. Richardson, J. Lee, and N. A. Kotov, "Gold nanoparticle ensembles as heaters and actuators: melting and collective plasmon resonances," Nanoscale Res. Lett. **1**, 84 (2006).

[152] C. R. Crick, P. Albella, B. Ng, A. P. Ivanov, T. Roschuk, M. P. Cecchini, F. Bresme, S. A. Maier, and J. B. Edel, "Precise attoliter temperature control of nanopore sensors using a nanoplasmonic bullseye," Nano Lett. **15**, 553–559 (2015).